Fall 2016

Spectroscopic and spectro-astrometric analysis of T Tauri Stars

Logan Ryan Brown

Department: Physics

SPECTROSCOPIC AND SPECTRO-ASTROMETRIC ANALYSIS OF T TAURI STARS

by

LOGAN RYAN BROWN

A DISSERTATION

Presented to the Faculty of the Graduate School of the

UNIVERSITY OF MISSOURI ST. LOUIS

and

MISSOURI UNIVERSITY OF SCIENCE AND TECHNOLOGY

In Partial Fulfillment of the Requirements for the Degree

DOCTOR OF PHILOSOPHY

in

PHYSICS

2016

Approved by

Erika Gibb, Advisor
Bruce Wilking
Paul Parris
Alexey Yamilov
Sean Brittain

ABSTRACT

To understand our own solar origins, we must investigate the composition of the protoplanetary disk from which the solar system formed. To infer this, we study analogs to the early solar system called T Tauri stars. These objects are low-mass, pre-main sequence stars surrounded by circumstellar disks of material from which planets are believed to form. We present high-resolution, near-infrared spectroscopic data for the T Tauri stars DR Tau and AA Tau using NIRSPEC at the Keck II telescope. For DR Tau, a spectro-astrometric analysis was performed, obtaining sub-seeing spatial information on water emission. Alongside a disk model, we constrained the viewing geometry of the disk (position angle ~140^{o}, inclination ~13^{o}) and the emitting region of the water emission lines (~0.056 – 0.38 AU). For AA Tau, we observed a superposition of strong water and OH absorption and emission features from two separate years, 2010 and 2014. During that time frame, AA Tau went through a dimming event, the effects of which we analyzed and used to discuss the implications for the source of the dimming event.

ACKNOWLEDGEMENTS

I gratefully acknowledge support from the NASA-Missouri Space Grant Consortium, the University of Missouri St. Louis's College of Arts & Sciences for a dissertation writing fellowship, NSF's Stellar Astronomy program, and the American Recovery and Reinvestment Act of 2009 (NSF 0908230), JPL (RSA No: 1423736), and the NASA Exobiology and Evolutionary Biology program (NNX07AK38G). I also acknowledge the contributions made by undergraduate and graduate research assistants Bryant Dentinger, Nick Kraftor, and Nathan Roth, as well as those made by my advisor, Dr. Erika Gibb, and collaborators, Dr. David Horne and Dr. Matthew Troutman. Data presented herein were obtained at the W. M. Keck Observatory, which is operated as a scientific partnership among the California Institute of Technology, the University of California, and the National Aeronautics and Space Administration. The Observatory was made possible by the generous financial support of the W. M. Keck Foundation. I recognize and acknowledge the very significant cultural role and reverence that the summit of Mauna Kea has always had within the indigenous Hawaiian community. Lastly, I would like to extend a thanks to all other members of my dissertation committee.

TABLE OF CONTENTS

Page

LIST OF ILLUSTRATIONS

LIST OF TABLES

1. INTRODUCTION

To understand how life originated on Earth, the origins of the Earth and the solar system must first be understood. General knowledge of star formation gives insight into the circumstances surrounding our solar system formation, and the discovery of over 3400 exoplanets[1], a number growing nearly every day, gives an ever expanding understanding of how we came to be. However, the process of planet formation is not well understood, particularly as it relates to the transition from a young, protostar surrounded by a disk of gas and dust to a full-fledged planetary system. Of particular interest is exploring the conditions present during the formation of stars analogous to the young Sun.

When the Sun was a young, pre-main-sequence star, it was surrounded by a large dust- and gas-rich protoplanetary disk with a mass on the order of tens of Jupiter masses and extending outward to about 100 AU from which our solar system formed (Vicente & Alves 2005). The investigation of how the necessary water and other prebiotic molecules were distributed through the protoplanetary disk of the early solar system is paramount to understanding our origins. One important question is how and when terrestrial planets like Earth acquired water and organic volatiles. A commonly invoked scenario suggests that volatile rich minor bodies (i.e., asteroids and comets) originating >~ 3-5 AU from the young Sun may have been transported to the inner protoplanetary disk via gravitational scattering by the giant planets where some impacted terrestrial planets (Morbidelli et al. 2000, Raymond et al. 2004, Walsh et al. 2011, O'Brien et al. 2014). Studying the

[1] http://exoplanetarchive.ipac.caltech.edu/

molecular gas in the inner (<5 AU) region of disks is key to understanding the formation of terrestrial planets and the transport of volatile material in disks. This introductory Section shall provide an overview of how stars form (Section 1.1), along with basic insights into the types of objects discussed in Sections 3 & 4, T Tauri Stars and protoplanetary disks (Sections 1.2 and 1.3), and the subjects of interest concerning these objects, disk chemistry and water (Sections 1.4 and 1.5).

1.1. STAR FORMATION OVERVIEW

In the spaces between stars, the so-called interstellar medium (ISM), are clouds of gas and dust of varying sizes, densities, and temperatures. These range from "diffuse" clouds with temperatures of ~30 – 80 K and densities of ~100 – 800 cm^{-3} to "dense" molecular clouds with temperatures of ~10 K and densities that exceed 10^3 cm^{-3}. Within these dense giant molecular clouds are clumps of higher density, known as dense cores, that are precursors to stars (Whittet 2002). The dense cores, under correct conditions, can slowly begin to accrete matter from the surrounding material, eventually collapsing due to a trigger event such as a shock wave or upon reaching a critical mass and collapsing under their own gravity. This leads to the formation of a high density central region surrounded by an envelope of lower density material.

Matter continues to accrete onto the central region and surrounding material, with the entire dense core continuing to contract. As the radius grows smaller and smaller, conservation of angular momentum increases the rotation rate. The bulk of the material rotates about a common vertical axis, with particle collisions eliminating motion in the vertical direction. Conservation of energy begins to heat the dense core as the high

density central region continues to collapse. What is then left behind is a dense central region forming a protostar and surrounding material flattening into a protoplanetary disk.

Matter from the surrounding envelope of material continues to accrete onto this new protostar/disk system. The protostar will accrete matter from the newly formed disk, and the interaction between protostar and infalling material results in outflows of gas along the axis of rotation (e.g., Reipurth & Heathcote 1991, Watson et al. 2016). Within the disk, planet formation begins through matter accreting into clumps (e.g., Brauer et al. 2008), the self gravity of the gas altering the structure of the disk and causing fragmentation (e.g., Johansen et al. 2006, Cuzzi et al. 2008, Dipierro et al. 2015a), or some combination of those two mechanisms. Eventually, conditions within the protostar become such as to start fusion within its core, finally entering the main sequence and becoming a true star. Stellar winds from the young star, alongside the collisions of bodies within the disk, removes the vast majority of remaining envelope of gas and dust, leaving behind a new star system (e.g., Simon & Prato 1995, Wolk & Walter 1996, Clarke et al. 2001, Alexander et al. 2006).

1.2. T TAURI STARS

T Tauri stars, with a mass similar to the Sun, are the closest analogs we have to the early solar system, and the protoplanetary disks found around these stars may hold clues to planet formation processes and timescales. They are the youngest, <~10 Myr, of the F, G, K, and M spectral type stars. They have masses up to 2 M_{sun} and cooler surface temperatures to main sequence stars of the same spectral type, though with greater luminosity due to their large radii (>~2R_{sun}) (Bertout 1989, Bergin et al. 2003, Preibisch

et al. 2005). Hydrogen fusion does not occur in their cores due to low core temperature so they are powered by gravitational energy and some deuterium burning as the star collapses. Highly active, T Tauri stars exhibit strong thermal X-ray and non-thermal far ultraviolet (FUV) radiation, as well as intense stellar winds (Bertout 1989, Bergin et al. 2003, Preibisch et al. 2005). Around these objects are large dust- and gas-rich disks of material known as circumstellar or protoplanetary disks.

1.3. PROTOPLANETARY DISKS

Protoplanetary disks are flattened, rotating disks of dust and gas around newly formed stars and potentially present observable initial conditions for planet formation. An inevitable consequence of conservation of angular momentum during the gravitational collapse of a cloud, these disks begin their lives rapidly funneling material onto the star until the surrounding molecular core becomes exhausted or disperses (Yorke et al. 1993, Hueso & Guillot 2005). From there, small amounts of disk material persist with masses on the order of tens of Jupiter masses and extending outward to about 100 AU with outliers having been observed with radii of up to a few hundred AU (Vicente & Alves 2005). These disks also exhibit a flared geometry (Kenyon & Hartmann 1987, Burrows et al. 1996, Stapelfeldt et al. 1998, Padgett et al. 1999, Smith et al. 2005).

The existence of protoplanetary disks has been historically evidenced from a number of observational considerations and were originally proposed by Immanuel Kant in 1755[2]. Inferred from the theory of stellar formation (e.g., Shakura & Suynaev 1973), available information on our own solar system, and modeling of the early solar nebula,

[2] Published in *Universal Natural History* and *Theory of the Heavens*

protoplanetary disks can be observationally inferred from their spectral energy distribution (SED). An excess of emission from the optical to the millimeter compared to the stellar continuum can be attributed to emission from a flat and geometrically thin distribution of gas and dust. In the 1990's, advances in adaptive optics in ground based telescopes and the Hubble Space Telescope allowed for the first direct observations of a protoplanetary disk in silhouette against the background light in the Orion Nebula (McCaughrean & O'Dell 1996). In addition, by mapping the CO J = 1–0 and J = 2–1 line emission from the gas, large millimeter arrays such as OVRO or the IRAM interferometers clearly demonstrated that the circumstellar material has a flattened structure and is in Keplerian rotation (Dutrey et al. 2004).

Protoplanetary disks around low-mass stars have typical lifetimes of ~10^6 years (Haisch, Lada & Lada 2001, Whittet 2002), which only allows one to study the evolution of these objects by performing observations on a statistically significant sample size of populations. The evolution of disk structure and the disk longevity is tied to angular momentum conservation due to continued accretion onto the star, photoevaporation from the central star and external stars, disk winds, and by the eventual agglomeration of dust grains into planetesimals large enough to gravitationally perturb the disk. These factors determine the planet formation environment of the disk, setting such factors as the location of the snow line, the mass and time available to form gas giants, and the rate of migration. These evolutionary factors lead to inner holes and gaps and the transition into becoming a debris disk: a dusty gas-poor structure whose properties reflect the collisional evolution of a population of small bodies (Wyatt 2008). Debris disks and their structure have most recently been observed in detail with ALMA (ALMA Partnership et al. 2015).

1.4. DISK CHEMISTRY

A wide range of temperatures are observed in protoplanetary disks – hot near the star, cooler farther away - allowing for observable wavelengths from microns to millimeters. These disks also exhibit vertical structure, as depicted in Figure 1.1, with distinct internal regions defined by their chemistry. While direct observations probe the chemical make-up of these disks, modeling gives insight into the expected molecular structure and helps provide a description of chemical layers of disks (Willacy & Woods 2009; Najita et al. 2011; Heinzeller et al. 2011; Walsh et al. 2015). These chemical zones of a protoplanetary disk can be summarized as follows: (1) cold midplane, a cold dense region beyond ~ 3 AU (the snow line), where molecules freeze onto dust grains; (2) the warm molecular layer above that, where molecular synthesis is stimulated by increasing temperatures and the evaporation of molecules from dust grains; and (3) the hot ionized disk atmosphere at the surface, where stellar and cosmic radiation dissociates and ionizes molecules into constituent radicals, atoms, and ions (e.g. Aikawa & Herbst 1999, Walsh et al. 2010).

The photon-dominated surface region of the disk is typified by dissociation and ionization. Stellar and cosmic radiation lead to the production of various ions, such as H_3^+, and bond restructuring processes drive ion-molecule chemistry (for example, $H_3^+ + CO \rightarrow HCO^+ + H_2$) and charge transfer reactions (for example, $He^+ + H_2O \rightarrow He + H_2O^+$). These processes are strongly dependent on the radiation field present. In T Tauri stars, the accretion shock emits intense non-thermal UV radiation in a pronounced Lyman α line (Herczeg et al. 2002, Schindhelm et al. 2012). These Lyman α photons selectively dissociate HCN and H_2O while leaving other molecules, such as CO and H_2, unaffected

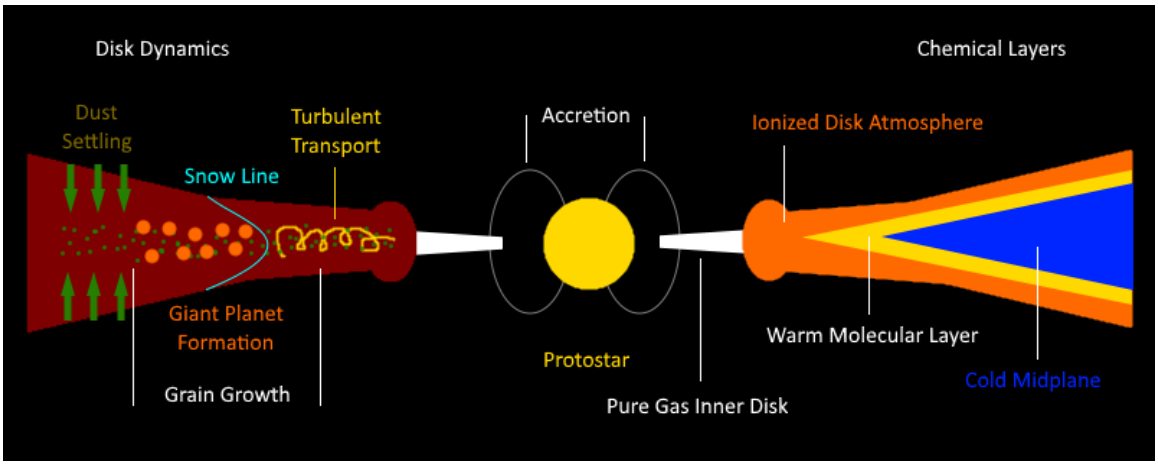

Figure 1.1. A depiction of the physical and chemical structure of a protoplanetary disk.

(van Dishoeck et al. 2006) but CO and H_2 can be photodissociated by FUV radiation (van Dishoeck et al. 2006, van Dishoeck & Black 1988). T Tauri stars also emit X-ray radiation generated by coronal activity, similar to our Sun, which produces chemically active He^+ that can destroy CO molecules, freeing carbon and oxygen for hydrocarbon chemistry (Henning & Semenov 2013).

Partially shielded from UV/X-ray radiation by the atmosphere, a warm layer of rich molecular chemistry is found below the disk surface. Gas-phase interactions, involving predominately neutral-neutral reactions, dominate here with thermal and non-thermal desorption of molecules from dust grains that are transported up from the cold midplane (Walsh et al. 2010). Thermal desorption occurs when the dust-grain temperature exceeds the freezeout temperature of the molecule, while non-thermal desorption is induced by penetrating cosmic rays, UV radiation, and X-rays (Walsh et al. 2010).

Within the interior of the disk, along the midplane at a distance beyond about 3 AU, is a cold dense region almost completely shielded from high-energy radiation (sans cosmic rays) where most molecular species are frozen onto dust grains. The primary

source of depletion comes from the freeze out of molecules at snow lines where temperatures are low enough for molecules to stick to the surfaces of dust grains near the midplane. The chemistry in the cold midplane is dominated by grain surface reactions. In regions where the temperature is sufficiently low and the H number density is sufficiently high, these are predominantly H addition reactions that lead to fully hydrogenated species like NH_3, C_2H_6, and CH_4. However, other reactions are possible. For example, OH (from photodissociated H_2O ice) can also react with CO to form CO_2, which is abundant in both interstellar and cometary ices (Walsh et al. 2015). While cosmic rays are mostly attenuated by the dust, there is a non-negligible contribution that can penetrate and create FUV photons by photoionizing H_2. The location where this freezeout of a molecule occurs defines "snow lines." For example, this happens for water at 2 – 3 AU in the early solar nebula and a CO snow line forms at about 20 AU (Morbidelli et al. 2000, Lecar et al. 2006, Encrenaz 2008, Min et al. 2011).

Table 1.1 adapted from Henning & Semenov (2013) summarizes a portion of the chemical reactions active in disks. Table 1.2 further summarizes chemical reactions active in disks but those specifically related to water in the hot ionized disk atmosphere. CO gas has been studied in disks for many years, but it is only recently that water and simple organic molecules such as HCN, C_2H_2, and CH_4 have been detected in the inner regions of T Tauri disks. This has been done using both the Spitzer Space Telescope (e.g., Najita et al. 2013; Carr & Najita 2011, 2008; Salyk et al. 2011; Pontoppidan et al. 2010) and ground-based, high-resolution, near-infrared spectroscopy (Gibb & Horne 2013; Mandell et al. 2012; Gibb et al. 2007; Lahuis et al. 2006). Most recently, the Atacama Large Millimeter/submillimeter Array (ALMA) has begun reporting detection

Table 1.1. Chemical Reactions Active in Disks

Process	Example	Mid-plane	Molecular layer	Atmosphere
Bond formation				
Radiative association	$C^+ + H_2 \rightarrow CH_2^+ + h\nu$	X	X	X
Surface formation	$H + H \parallel gr \rightarrow H_2 + gr$	X	X	O
Bond destruction				
Photodissociation	$CO + h\nu \rightarrow C + O$	O	X	X
Dissociation by CRP	$H_2 + CRP \rightarrow H + H$	X	X	O
Dissociation by X-rays	--	O	X	X
Dissociative recombination	$H_3O^+ + e^- \rightarrow H_2O + H$	X	X	X
Bond restructuring				
Neutral-neutral	$O + CH_3 \rightarrow H_2CO + H$	X	X	O
Ion-molecule	$H_3^+ + CO \rightarrow HCO^+ + H_2$	X	X	X
Charge transfer	$He^+ + H_2O \rightarrow He + H_2O^+$	X	X	X
Unchanged bond				
Photoionization	$C + h\nu \rightarrow C^+ + e^-$	O	X	X
Ionization by CRP	$C + CRP \rightarrow C^+ + e^-$	X	X	O
Ionization by X-rays	--	O	X	X

Note – X denotes process is present, O denotes process is absent. Adapted from Henning & Semenov (2013).

of organics in protoplanetary disks, such as complex cyanides similar in composition to what is observed in comets (Öberg et al. 2015). Many other molecules are predicted to be abundant in disks but have only upper limits reported for them (Bast et al. 2013).

1.5. WATER IN DISKS

As our ability to observe protoplanetary disks has improved so too has the understanding of water in these objects. Gas-phase chemistry in the hot, inner disk region (T > 300K) locks up the majority of oxygen in water through reactions between molecular hydrogen with oxygen or OH,

Table 1.2. Water Related Processes

Process	Example
H_2 formation	
Radiative attachment	$e + H \rightarrow H^- + h\nu$
	$H^- + H \rightarrow H_2 + e$
Three-body reaction	$3H \rightarrow H_2 + H$
	$2H + H_2 \rightarrow 2H_2$
OH formation	
Neutral radical reaction	$H_2 + O \rightarrow H + OH$
H_2O formation	
Exothermic reaction	$H_2 + OH \rightarrow H + H_2O$
O_2 formation	
Exothermic radical reaction	$O + OH \rightarrow O_2 + H$
CO formation	
Exothermic radical reaction	$C + OH \rightarrow CO + H$
OH & H_2O destruction	
Charge transfer	$H^+ + H_2O \rightarrow H_2O^+ + H$
	$H^+ + OH \rightarrow OH^+ + H$

Note – Adapted from Glassgold, Meijerink, and Najita (2009).

$$H_2 + O \rightarrow H + OH, \quad H_2 + OH \rightarrow H + H_2O, \tag{1.1}$$

and water and OH have been extensively observed in a variety of objects (e.g., Pontoppidan et al. 2010, Salyk et al. 2008, Carr & Najita 2008). Desorption of water from icy grain mantles is also a major contributor to gas-phase water in the outer disk (> ~1 AU). In either case, the water fractional abundance relative to total gas reaches values as high as ~10^{-4} (Nomura et al. 2012, Walsh et al. 2015). Reactions of a much lower efficiency also form water in the cold outer disk via hydrogenation of oxygen through ion-neutral reactions,

$$O \xrightarrow{H_3^+} OH^+ \xrightarrow{H_2} H_2O^+ \xrightarrow{H_2} H_3O^+ \xrightarrow{e^-/gr^-} H_2O. \tag{1.2}$$

Water in disks can also be observed as ice frozen to grains in the cold midplane and outer regions of the disk (Hogerheijde et al. 2011, Honda et al. 2009, Terada et al. 2007). This water ice can be a result of gas-phase water from the inner disk being transported to cold regions, either radially outward or toward the midplane (for regions > ~3 AU), where it freezes out onto dust grain surfaces. Water ice can also be formed via grain surface reactions where atomic hydrogen and oxygen have become stuck to a grain surface. These atoms migrate on the grain surface until they combine to form OH and H_2O, and unlike H_2, which releases energy upon formation resulting in its ejection from the grain surface, the higher binding energy of hydrogenated products allows them to remain attached to the grain surface, forming icy mantles. Some of the water ice present in the molecular cloud prior to collapse may survive in regions beyond 10 AU from the protostar, which helps facilitate the survival of solid CO as part of mixed CO-H_2O ices at temperatures above 18 K, a fact important for helping to explain CO ices in comets (Visser et al. 2009, Drozdovskaya et al. 2016).

1.6 SUMMARY

This dissertation is focused on observations of two Classical T Tauri stars, DR Tau and AA Tau. High resolution, near-infrared data were collected for these sources. In the case of DR Tau, said collection was optimized for the use of spectro-astrometry (SA; see Section 3 and appendix A). This optimization not only allows a SA analysis to be performed on the data, but the high signal to noise ratio resulting from the long integration time necessary to perform SA allows for the potential of a detailed, conventional analysis of the spectroscopic data. AA Tau data collection was done to

measure volatile composition in inner protoplanetary disk regions, with spectroscopic modeling done to analyze observed emission and absorption. Discussion of the observation of these objects and the data reduction can be found in Section 2. Section 3 presents the analysis of DR Tau and SA, while Section 4 focuses on the analysis of water and OH within AA Tau's disk and AA Tau observations during several epochs.

2. OBSERVATIONS AND DATA REDUCTION

The primary means through which the chemistry of protoplanetary disks, and star formation in general, is studied is spectroscopy. Spectroscopy provides unprecedented information concerning observed objects when all that is available to an observer is the light emitted from the object in question. By comparing synthetic models to observations, the composition and temperature of both emitting material and absorbing material between the observer and an object can be determined.

Given that star formation regions predominantly radiate in the infrared and Earth's atmosphere features strong absorption there, infrared observations often necessitate airborne or space-based telescopes, with early contributions to infrared astronomy from the Kuiper Airborne Observatory (KAO; in service 1974 - 1995), the Infrared Astronomical Satellite (IRAS; launched in 1983), and the Infrared Telescope in Space (IRTS; operated during 1995). The field was later revolutionized by the Infrared Space Observatory (ISO; mission lasted from 1995 - 1998) allowing for the first comprehensive study of star formation regions. Current space-based instruments such as the Spitzer Space Telescope and ground based facilities such as SpeX at the NASA Infrared Telescope Facility (IRTF), the Near-Infrared Spectrograph (NIRSPEC) at the Keck II observatory, and the Atacama Large Millimeter/submillimeter Array (ALMA) have provided continuing and invaluable data of T Tauri stars and protoplanetary disks. Here we have utilized NIRSPEC on Keck II for our observations.

2.1. OBSERVATIONS

The W. M. Keck Observatory is located on the summit of Hawaii's dormant Mauna Kea volcano, consisting of a pair of 10 m optical and infrared telescopes, the largest such optical telescopes in the world (McLean et al. 1998). The telescope's primary mirrors consist of 36 hexagonal segments that work together as a single unit. Keck II features a wide array of instruments, of which we used NIRSPEC, a cross-dispersed high-resolution cryogenic echelle spectrograph, which results in a resolving power of $\lambda/\Delta\lambda \sim 25{,}000$.

High-dispersion, near-infrared (NIR) spectroscopic data from the T Tauri star AA Tau were obtained on 2010 February 23 and 2014 September 6 and the T Tauri star DR Tau on 2011 February 16-18 using NIRSPEC. The observations for both AA Tau and DR Tau range from 2860 cm^{-1} (3.50 μm) to 3455 cm^{-1} (2.88 μm), though the 2014 AA Tau observations do not have complete coverage over that range (see Section 4 for more details). The spectral ranges were chosen to cover many transitions of both OH and H_2O. Observations were performed with the 3 pixel (0.″43) wide slit, and we used a standard ABBA nod pattern, with a 12″ beam separation along the 24″ long slit. In the case of DR Tau, observations were optimized for spectro-astrometry, viewing the source at three different position angles (PA) and their 180^o offsets (Brannigan et al. 2006). Table 2.1 contains the observing information.

2.2. DATA REDUCTION

NIRSPEC is a cross-dispersed instrument, allowing for a large spectral range to be observed by splitting it into several orders, physical rows on the detector, which were

Table 2.1. Observing Log

Object	Date	Setting	P.A. (^{o})	Int. Time (min.)
DR Tau	16 Feb 2011	KL2	-70	28
			-40	16
			-10	16
			+50	16
			+110	16
			+140	16
			+170	20
	17 Feb 2011	KL1	-70	16
			-40	20
			-10	20
			+110	16
			+140	16
	18 Feb 2011	KL1	+50	16
			+170	16
AA Tau	23 Feb 2010	KL1	N/A	36
		KL2	N/A	24
	6 Sept 2014	KL2	N/A	36

selected and processed individually. Taking advantage of the ABBA nod pattern and combining the spectra of the two beams as (A – B – B + A) cancels, to second order, emissions from "sky" lines and thermal background. Data were dark subtracted and flat fielded, and they were cleaned of high dark current pixels and cosmic ray hits.

The data do not fall linearly across the detector, requiring us to both spatially and spectrally straighten the data. Spatial straightening is achieved by first determining the peak position of the star by fitting a Gaussian to each column of the given order. From there, a polynomial is fit to the peak positions, which was then used to place the data horizontally. Spectral straightening was achieved through a row-by-row comparison to the telluric emission lines.

From there, atmospheric absorption must be accounted for since the ABBA method accounts for the majority of the sky emission, not absorption. An atmospheric transmittance function was modeled using the Line-By-Line Radiative Transfer Model

(LBLRTM, Clough et al. 2005), which was optimized for Maunakea's atmospheric conditions (see Villanueva et al. 2011). For each setting, the abundances of atmospheric species, the spectral resolving power, and the wavelength calibrations were established by fitting the optimized model to the data. To extract the spectral features, the convolved telluric models were subtracted from the extracted spectra. An example of the resulting residuals, which are still convolved with the transmittance, alongside the original reduced spectra and the telluric model can be found in Figure 2.1.

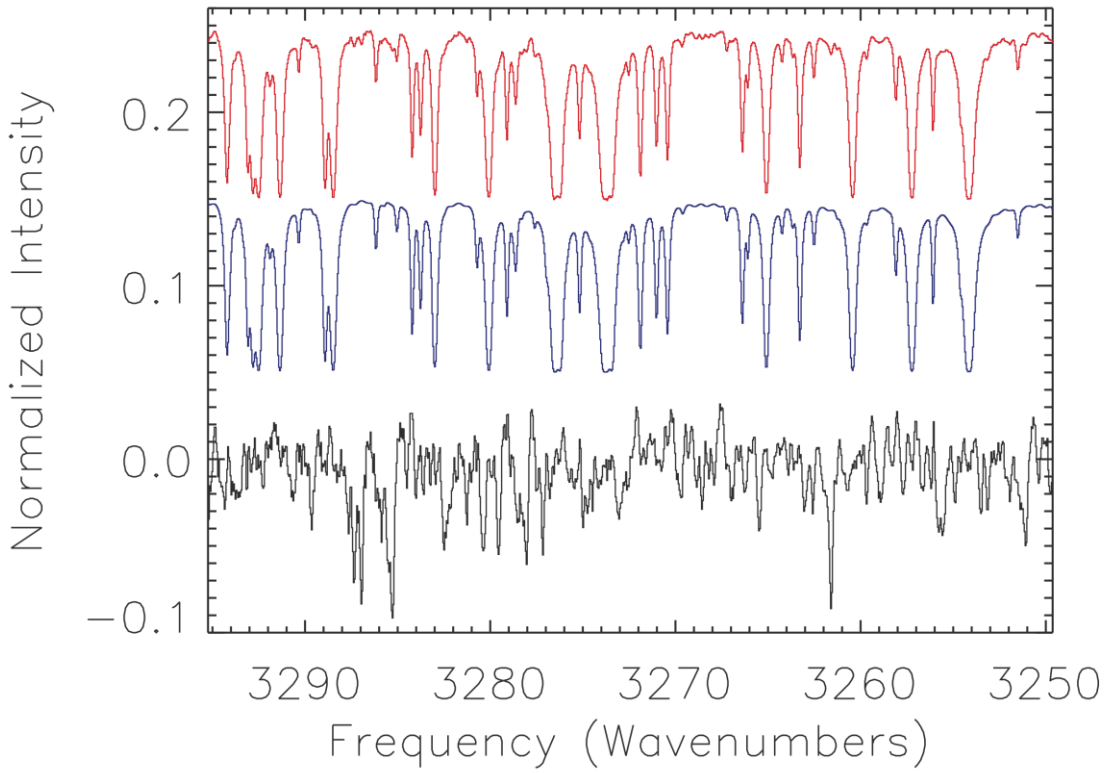

Figure 2.1. An example spectrum from the 2010 observation of AA Tau; a reduced spectrum (red), the best-fit telluric model (blue), and the resulting residual (black). The spectra and telluric models have been scaled down by a factor of 10.

3. SPECTRO-ASTROMETRY OF WATER IN DR TAU

DR Tauri is a typical example of a classical T Tauri star. Located at a distance of about 140 pc, DR Tau has a spectral type of K5 with a T_{eff} = 4500 K and total visual extinction $A_v \sim 1.6$ (Muzerolle et al. 2003, Johns-Krull & Gafford 2002). A well-studied object, DR Tau is known to have a circumstellar disk. Our primary goal with DR Tau was to determine the spatial extent of observed molecular emission from water. To accomplish this task, we used the technique of spectro-astrometry.

Spectro-astrometry is a technique that utilizes high-resolution spectrometers with excellent imaging quality to obtain sub-seeing and sub-diffraction limited spatial information from emission lines originating in non-uniform objects, such as circumstellar disks (Beckers 1982, Christy et al. 1983, Aime et al. 1988, Bailey 1998, Acke et al. 2005). Using this technique, it is possible to constrain the spatial distribution of an emitting molecule on sub-AU scales at the distance of DR Tau, as well as the position angle (PA) of the disk on the sky and its inclination (Pontoppidan et al. 2008, 2011; Whelan & Garcia 2008; Brittain et al. 2009; van der Plas et al. 2009). A full discussion of the spectro-astrometric technique can be found in Appendix A.

We present high-resolution, near-infrared, SA observations of DR Tau, centered near 3 μm. DR Tau is relatively bright in the near-infrared and exhibits a rich emission line spectrum (Salyk et al. 2008; Mandell et al. 2012). We detected many water and OH emission features originating in the disk. While an SA analysis was attempted for both water and OH, only the water lines produced a signal. Here we report our SA analysis for the water lines.

3.1. SPECTRO-ASTROMETRIC ANALYSIS

The projected velocity of gas in a rotating disk varies as a function of orbital phase and distance from the star. Regions of common projected velocity space map in loop-like structures. Thus the point spread function (PSF) of each velocity channel of a resolved emission line formed in the disk is offset from the position of the star. While the typical image quality of standard NIR observations is ~0.5 pixel, SA observations can be used to determine the centroid of the PSF to ~0.005–0.010 pixel. At the distance of DR Tau (~140 pc), this provides a spatial resolution <1 AU. Once the beam centers were determined, the centroid for each pixel in frequency space was calculated; this "center-of-light" calculation is analogous to a center-of-mass calculation. We adopted the method of Pontoppidan et al. (2008), calculating the centroid as follows:

$$X_n(v) = C\frac{\sum_i (x_i(v) - x_o)F_i(v)}{\sum_i F_i(v)}, [pixels] \quad (3.1)$$

where C is a correction factor based on the amount of flux not included in the window over which the signal is calculated and is a number of the order of unity. X_v is the spatial offset (the SA signal; see Figure 3.1), x_i is the position of a given pixel, x_o is the centroid of the star, and F_i is the flux for pixel i at a specific wavenumber. This signal is diluted by the strength of the feature relative to the continuum. The undiluted signal is calculated as follows:

$$X_{undiluted} = X_n(1 + \frac{F_{cont}}{F_{line}}) \quad (3.2)$$

The spatial offsets for each beam were averaged together to produce the signal for each straightened frame. The signals for each frame were then averaged to create the signal for a given PA. Each signal was combined with its 180◦ offset. Pairwise subtracting of the

parallel and antiparallel SA signals removes artifacts from reduction and instrumental effects without removing any real signal, i.e., $(X_0–X_{180})/2$. A detailed description of the SA analysis can be found in Appendix A.

3.2. MODELING THE SPECTRO-ASTROMETRIC SIGNAL

Emission from a disk in Keplerian motion is expected to produce an antisymmetric SA signal, with the blue- and redshifted sides of the line offset in opposite directions. The H_2O position-velocity diagrams of the averaged feature and signals for DR Tau are shown in Figure 3.1. The observed lines were resolved beyond the instrument profile and were identified via the HITRAN database (Rothman et al. 2009, 2013).

In order to interpret the observed SA signal and determine the spatial extent of water emission, we modeled a disk that assumes a flat, circular slab rotating with simple Keplerian motion. An adaptive mesh was used to divide the modeled disk into pieces such that any radial step or angular step moves no more than a set model resolution in velocity space. Each of these calculated regions was treated as its own emitting black body. Mandell et al. (2012) found that an exponential drop off in flux ($\propto R^{-3}$) provided a better fit to the OH emission profile of T Tauri star RU Lup. Such an exponential decrease in flux is also consistent with the outer radius limit for water and OH (~0.5 AU) determined by Pontoppidan et al. (2011) for AS 205N. For this reason, we adopted a flux of $R^{-\beta}$ with a β value of -3 for our modeling (see Table 3.1). A constant radial surface density was assumed.

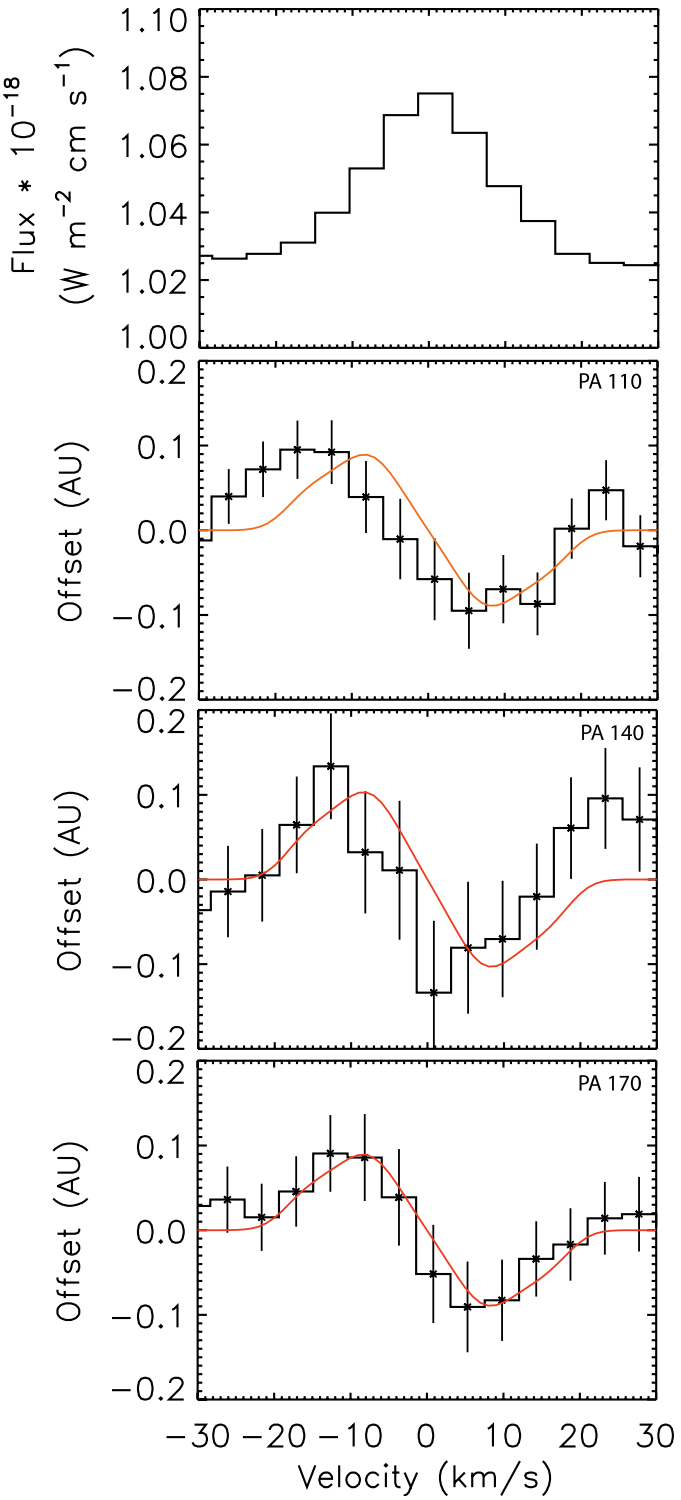

Figure 3.1. The top panel shows the average emission profile in velocity space of three strong H_2O 001-000 vibrational transition lines (centered at 3321.56 cm^{-1}, 3415.51 cm^{-1}, 3426.19 cm^{-1}) that generate spectro-astrometric signals. The bottom three panels are the averaged SA signals (X_n) for those features (black lines) for each slit P.A. and 180° offset with the best-fit model over plotted (red line). The horizontal axis is in velocity space (km s^{-1}). 1σ error bars are shown.

Figure 3.2 shows a contour plot of the line of sight velocity of the best-fit model disk projected on the sky. From the model, a synthetic spectral feature and its corresponding SA signal was generated, shown as the red lines in Figure 3.1.

The position angle, inclination, and the inner and outer emitting regions were varied to find the signal that best matched the data using a least chi-squared fit. For this work, we kept the stellar mass fixed, adopting the mass from Isella et al. (2009) of 0.4 $M_{\odot}$ (see Table 3.1). The position angle and inclination have a direct impact on the SA signal itself (see Appendix A) while the radius affects the flux term used to calculate the SA signal. The inner and outer radii that generate the best fit correspond to the spatial extent of emission for that feature. Table 3.1 shows a summary of the fixed and best-fit model parameters. We found that for the disk around DR Tau, the SA signal indicates that strong gas phase water emission originates in a region extending from 0.056 - 0.38 AU for a nearly face on disk (i ~ 13°). A detailed description of the modeling can be found in Appendix B.

3.3. DISCUSSION

Spectro-astrometry is a powerful technique for constraining both the disk geometry and the location of molecular emission in a proto-planetary disk. The reported geometries in the literature for the DR Tau disk are highly uncertain. PAs of 160^{o} (Akeson et al. 2005), 170^{o} (Andrews & Williams 2007), 98^{o} (Isella et al. 2009), and 0^{o} (Pontoppidan et al. 2011) have been cited, with our best-fit PA of 140^{o} falling within those values. Literature values for inclination also vary substantially, ranging from nearly face on (9°, Pontoppidan et al. 2011) to nearly edge on (69°, Muzerolle et al.

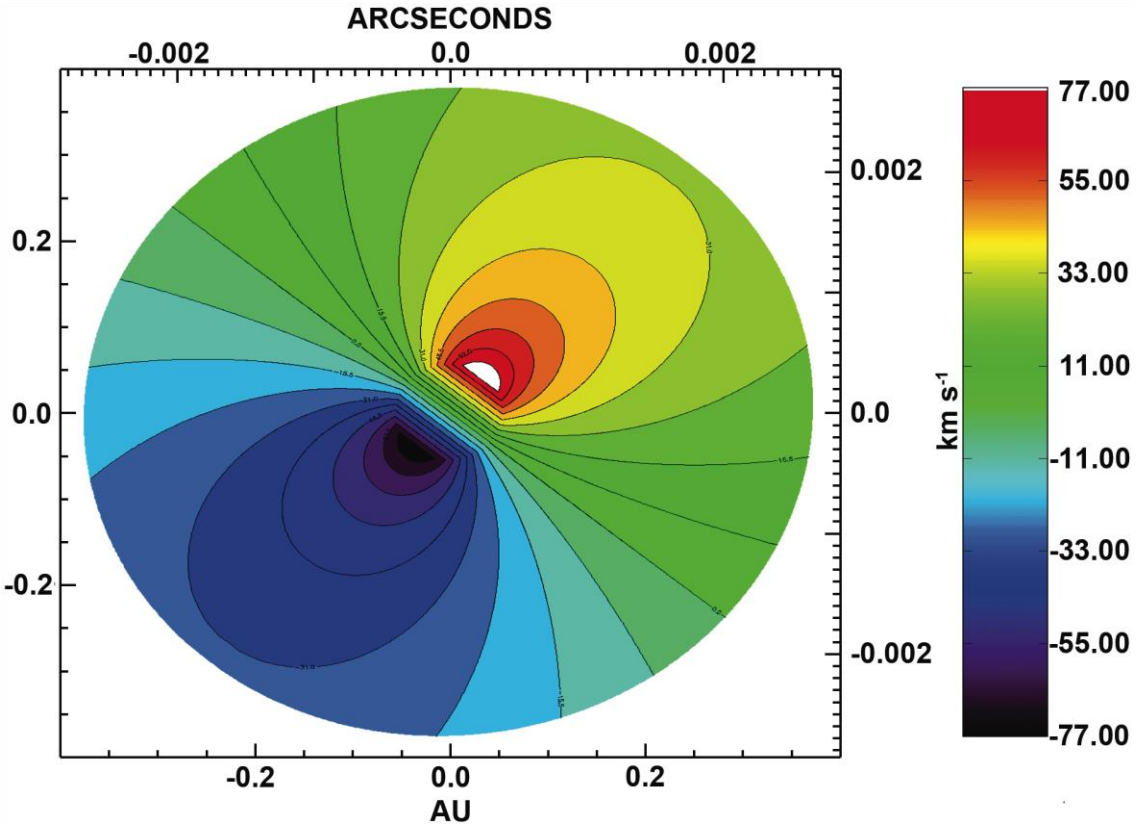

Figure 3.2. A projection of the modeled DR Tau disk on the sky, the area of which is the best fit emitting range. The contours are plotted for the line of sight velocity calculated by the disk model.

Table 3.1. Summary of Model Parameters

Beta[1]	P.A.[2] (°)	Inc.[3] (°)	Mass[4] ($M_\odot$)	R_{in} (AU)	R_{out} (AU)
3	140	13	0.4	0.056	0.38

NOTE. - (1) Mandel et al. 2012. (2) PA is degrees east of north. (3) Inclination is such that 0° is face on, 90° is edge on. (4) Isella et al. 2009.

2003) as well as intermediate values (36°, Isella et al. 2009). We found that a nearly face on orientation with an inclination of ~13° was required to fit the SA signal, in agreement with the inclination inferred by Pontoppidan et al. (2011) from spectro-astrometric analysis of CO. The nearly face-on orientation of DR Tau is consistent with the uncertainty in published position angles.

While Pontoppidan et al. (2011) detected a prominent CO SA signal for T Tauri star AS 205N, neither water nor OH exhibited SA signals. An upper limit for the water emitting region in the AS 205N disk of <~0.5 AU was determined, corresponding to an emitting area of <~0.8 AU^2. This value is consistent with the water emission region inferred by Salyk et al. (2008) for both AS 205N and DR Tau from modeling the spectroscopic emission features. In addition, the inner radius of emission we calculated is similar to that derived for the dust sublimation radius in DR Tau (Akeson et al. 2005), while the characteristic emitting radius correlates well with that for CO (Salyk et al. 2011). Our SA analysis of DR Tau indicated a water emitting region close to the star, with best fit values for the inner and outer emitting regions of 0.056 and 0.38 AU, respectively.

Are these values consistent with what would be expected from astrochemical modeling of protoplanetary disks? Water emission is expected to originate from a warm layer in the disk atmosphere (see models by Willacy & Woods 2009; Walsh et al. 2010; Najita et al. 2011; Heinzeller et al. 2011). While these models differ in their details, they are still useful for guiding interpretation of our measurements, especially when coupled with other spectroscopic measurements for DR Tau. Salyk et al. (2008) and Mandell et al. (2012) both modeled emission lines of water in DR Tau and found a gas temperature of ~900-1000 K. This temperature is typical of terrestrial planet forming regions and is consistent with the temperature of the disk where Walsh et al. (2010), Walsh et al. (2015), and Willacy & Woods (2009) predict a peak water fractional abundance in the disk atmosphere. In the case of Walsh et al. (2010), however, the water fractional abundance is still high beyond 10 AU. We note that many models do not include

mechanisms that may transport material from above the disk midplane beyond ~2-3 AU to the midplane where it can condense onto icy grain mantles (beyond the "snow line"). This effect is illustrated in Heinzeller et al. (2011) where radial viscous accretion, vertical turbulent mixing, and vertical disk winds were included, and a dramatic decrease in water fractional abundance in the disk atmosphere was predicted. More work must be done to model the complex chemistry and transport mechanisms that are expected to occur in protoplanetary disks, but our results suggest that most of the water emission is originating in the hot inner disk region.

We do note that while AS 205N showed a strong SA signal from CO but not water or OH, DR Tau exhibited a possible weak SA signal for CO (Pontoppidan et al. 2011) and a small water SA signal but no signal for OH. We also point out that the model fits to our water SA signal are not ideal, as Figure 3.1 clearly shows for all PA pairs that the model exhibits a slight (~3 km s^{-1}) blue shift from the observed signals. Additional factors may need to be included in our disk model, such as the disk wind suggested by Pontoppidan et al. (2011) to account for the discrepancy. However, our observed velocities do not necessarily lend credence to a disk wind. Bast et al. (2011) reported a heliocentric stellar velocity for DR Tau of 27.6 km s^{-1}, which combined with an Earth component as calculated for our date of observation (29.5 km s^{-1}), gives a geocentric velocity of 57.1 km s^{-1}. We observed a v(H_2O) of 56.0 km s^{-1} which in considering a 1 to 2 km s^{-1} uncertainty in the velocities, suggests only the slightest of disk winds or no disk wind at all.

Another possible explanation that can lead to an offset in the SA signal is asymmetrically distributed dust contributing strongly to the continuum. Since the SA

calculation is akin to a center of mass calculation, a disk of non-uniform gas and dust can pull the continuum centroid, or "center of light," away from the stellar position (though the Keplerian velocity field will remain centered about the star). Given the SA calculation here assumes a continuum centroid at the stellar position, this could result in the slight blue shift observed in the SA signals. Additionally, the low inclination could explain the observed single peaked features that have challenged interpretation of spectra (see for example Mandell et al. 2012), where a highly inclined disk produces peaks close together which may end up lost due to the resolution of the observations. Figure 3.3 illustrates a comparison of the spectral feature from Figure 3.1, a highly inclined modeled

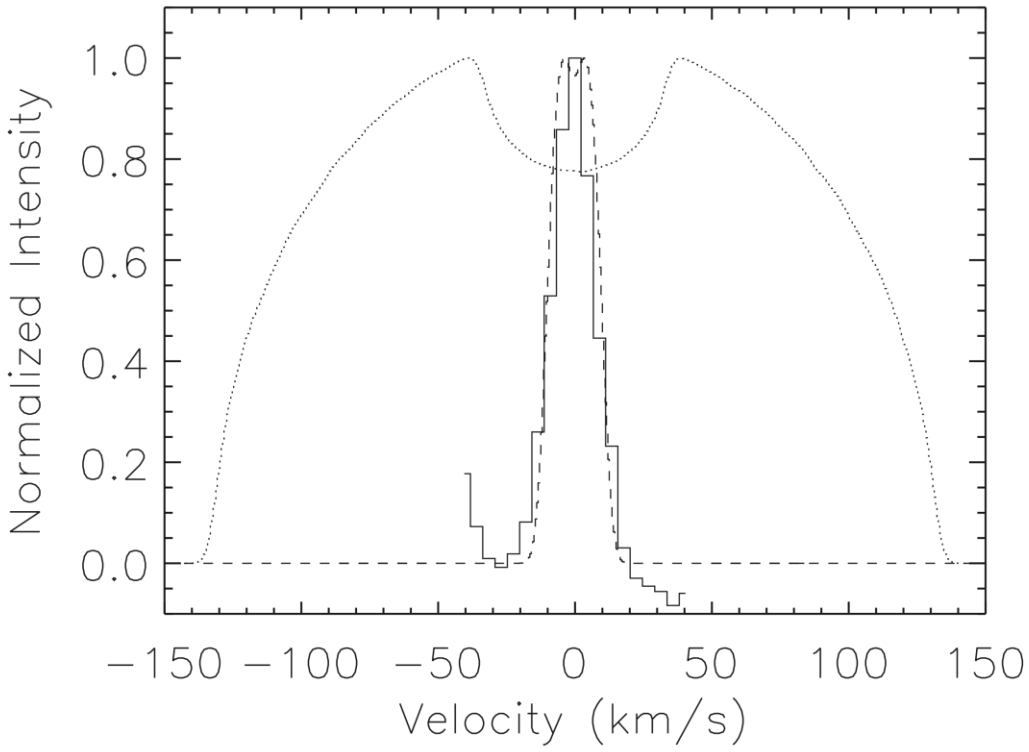

Figure 3.3. The solid line is the spectral feature from the top panel of Figure 3.1, normalized to arbitrary units of intensity. The dashed line is a modeled spectral feature using the DR Tau parameters as outlined in Table 3.1. The dotted line is a modeled spectral feature using the DR Tau parameters as outlined in Table 3.1 except with the disk inclination set to 85^{o}, a nearly edge on orientation. The results clearly show that the observed emission feature is more consistent with a face-on orientation, with the double peaked structure simply not being observed due to the resolution of the observations.

disk feature using the DR Tau parameters found in this work (dashed line), and a nearly edge on modeled disk feature (dotted line). The figure clearly indicates the emission line profile favors the face-on orientation, leading further credence to the inclination that we inferred based on the analysis of the SA signal.

4. NEAR-INFRARED SPECTROSCOPIC STUDY OF AA TAU

AA Tauri is another example of a typical classical T Tauri star. Located at a distance of ~140 pc, it is of spectral type K7 with a T_{eff} = 4000 K and A_v ~ 0.8 (Donati et al. 2010, Bouvier et al. 1999). A well-known object, AA Tau shows strong H_α emission and an infrared excess indicating the presence of a gaseous and dusty accretion disk (e.g. Bouvier et al. 1999).

AA Tau undergoes periodic eclipses caused by a warped inner disk structure, presumably caused by the magnetic field of the star (Bouvier et al. 1999, 2003, 2007). The periodic eclipses are used to calculate an equatorial rotation period (8.22 +/- 0.03 d; Bouvier et al. 2007). This equatorial velocity, coupled with a measured $v \sin i$ = 11.3 +/- 0.7 km s^{-1} (Bouvier et al. 2003), confirms a calculated inclination for the disk around AA Tau of $70^o \pm 10^o$ (Donati et al. 2010). This disk inclination was independently verified by Cox et al. (2013) through direct imaging of AA Tau. Fitting models of varying disk inclinations to the images, they found a best fit of $i = 71^o \pm 1^o$, in good agreement with Donati et al. (2010).

Nearly edge-on sources like AA Tau provide an opportunity to potentially probe the warm molecular layer of a protoplanetary disk (see Section 1.4). With this viewing geometry, cooler disk material is viewed against the stellar or hot inner disk continuum. AA Tau is known to lack a significant molecular envelope. Most of its absorption is likely to be from disk material close to the star (e.g. Carr & Najita 2008). Because of this, we acquired 3 micron data of AA Tau on 23 Feb 2010 as part of a study of water in protoplanetary disks. Additionally, observed emission from AA Tau also suggests that its

disk inclination is such that the line-of-sight through the disk material also permits viewing of hot disk emission, most likely from the surface as discussed below (see Section 4.2).

Interestingly, despite remaining at a nearly constant maximum brightness level (V ≈ 12.4 – 12.6 mag) for at least 24 years (Grankin et al. 2007), AA Tau's visual extinction suddenly increased by 4 mag in late 2011, and it has remained in this faint state through at least 2015 (Bouvier et al. 2013, Zhang et al. 2015, Schneider et al. 2015). One suggestion for the dimming is the presence of additional disk material in the line of sight toward the central source (see Section 4.4.2 below). To investigate the possible effect that the dimming event had on the water and OH absorption and emission, we acquired one L-band setting with NIRSPEC of AA Tau in September of 2014.

We present data acquired during two epochs of AA Tau, one before and one after the dimming event, analyzing and comparing near-infrared observations of AA Tau in 2010 and 2014. While our observations in 2010 covered a region ranging from 2860 cm^{-1} (3.50 μm) to 3477 cm^{-1} (2.88 μm), the 2014 observations had only one setting and thus did not provide complete coverage over the 2010 observations. Water and OH were analyzed to determine column densities and temperatures, and we investigated how they changed since the dimming event. Our results are compared with observations of CO performed by Zhang et al. (2015) and Schneider et al. (2015) since the dimming event began, where they also presented pre- and post-dimming data.

4.1. PHOTOSPHERIC ABSORPTION LINES

Late spectral type stars like AA Tau can potentially exhibit significant photospheric absorption lines in the near infrared, which must be removed or flagged prior to analysis of the circumstellar features. Therefore, in order to obtain accurate measurements from only the circumstellar contribution, we have expanded our analysis to incorporate photospheric models based on Kurucz grids of model atmospheres (Kurucz 1992). The use of these models to conduct in depth analyses of premain-sequence stellar photospheres over the respective gravity ranges of the sources covered in this paper is not unusual. The models and procedures employed in this study are based on well-established and accepted methods and have been shown to reproduce high quality, photospheric signatures in pre-main-sequence stars (see Hauschildt et al. 1999; Doppmann et al. 2005; Najita et al. 2008). Both Doppmann et al. and Najita et al. applied these models to isolate the signature of circumstellar CO in T Tauri objects using methods comparable to those presented in this paper.

Synthetic spectra were generated through use of the Spectrum stellar synthesis program (Sneden 1973) in conjunction with NEXTGEN stellar atmospheric models (Hauschildt et al. 1999) referencing the Kurucz atomic line lists (Kurucz 1979, 1993). The best fit to our observed spectrum was achieved using a temperature of T_{eff} = 4000 K and surface gravity of $log\ g \sim 3.7$ at a resolving power equal to that of the observed NIRSPEC data (~25,000). A least-squares minimization routine was employed to ensure the best possible fit between the observed spectra and the corresponding theoretical model. To accurately reflect the features of the observed spectra, the effects of extinction, rotational broadening, and veiling were incorporated into each model.

Atmospheric transmittance was applied to the models in the same manner as the observational data, using the output of the LBLRTM atmospheric model referencing the HITRAN 2012 molecular line database. Values for extinction (A_V) and rotational broadening ($v \sin i$) for AA Tau were retrieved from the existing literature where available and are summarized in Table 4.1. The model was reddened and rotational broadening was applied through convolution of the photospheric spectral lines with a line-spread function based on the value for $v \sin i$.

After compensation for the above effects, the modeled spectrum was used to represent the "unveiled" spectrum of the target star. Veiling reduces the depth of photospheric lines by enhancing the continuum level of the spectrum; this results in an underestimation of spectral lines' equivalent widths. The level of veiling or veiling factor of a T Tauri star may be quantified as the ratio of the flux generated by the surrounding environment to the photospheric flux:

$$r = \frac{F_{veil}}{F_{phot}} \tag{4.1}$$

In terms of normalized flux, this relates to the equivalent width as

$$1 + r = \frac{W_{phot}}{W_{veil}} \tag{4.2}$$

While the veiling toward AA Tau is likely dominated by an excess of infrared radiation originating from dust in the circumstellar disk, other factors may contribute to veiling in T Tauri stars. The shock region as material falls onto the star increases the local radiation budget, however this effect tends to peak in the ultraviolet. Accretion processes originating in the inner region of the accretion disk may also produce high-energy radiation. We have adopted the method of Hartigan et al. (1989) to determine the degree

Table 4.1. Summary of AA Tau Parameters

Inc. (°)[1]	A_v[2]	v sin i (km s^{-1})[3]	Spectral Type
71 ± 1	0.74	11.4	K7

NOTE. - (1) Cox et al. 2013. (2) Bouvier et al. 1999. (3) Bouvier et al. 2003.

of veiling in our data, where the veiling component of the observed flux is determined by fitting a standard spectrum plus a constant. This constant was then applied to the model. Veiling is relatively constant over small wavelength increments; hence, determination of veiling values on an order by-order basis minimizes the error within our fitting procedure.

The final model, adjusted for the above parameters, was then scaled to the observed data using a least-squares fit to ensure the best possible match to the data. The synthetic stellar model was then used to identify which transitions were potentially blended with strong stellar features. These were eliminated from our analysis. We also note that a separate photospheric model was not generated for the 2014 data set, using the one for 2010 to guide our analysis of the 2014 spectra. While the veiling and extinction are significantly different in 2014 versus 2010, the primary concern is noting line positions of photospheric features to guide our spectral fitting and avoiding potential photospheric lines in our analysis.

4.2. ANALYSIS & RESULTS

In both 2010 and 2014, AA Tau exhibited a rich spectrum of molecular emission and absorption lines dominated by ro-vibrational transitions of H_2O and OH. The geocentric Doppler shift of AA Tau at the time of the 2010 observations (~50 km s^{-1}) and 2014 observations (~-9 km s^{-1}) shifted many transitions into good transmittance. Lines

that were at good transmittance (>40%) and were not significantly blended with other species or with photospheric lines were included in the analysis.

Our Doppler shifts are in reasonable agreement with expected Doppler shifts based on the reported heliocentric Doppler shifts (km s^{-1}) of 16.1 ± 2 (Hartmann et al. 1986), 17.1 ± 0.9 (Bourvier et al. 2003), and 17.2 ± 0.1 (Donati et al. 2010). Assuming a heliocentric Doppler shift of 17.1 km s^{-1} for AA Tau and shifting to a geocentric frame accounting for Earth's orbital motion toward/away from AA Tau, the expected goecentric Doppler shifts (km s^{-1}) are 47 and -12.4 for 2010 and 2014, respectively, an approximately one pixel difference from the measured Doppler shifts (km s^{-1}) of 50 and -9. Interestingly, the data suggests that the water lines observed in 2014 appear to have a component requiring a Doppler shift of -3 km s^{-1} (see Section 4.2.4 below). Comparing our two data sets by removing Earth's Doppler shift and assuming nothing else changed, 2014 exhibited a 6 km s^{-1} redshift beyond what we would expect for many of the observed water lines.

To analyze the spectra, we generated synthetic local thermodynamic equilibrium (LTE) models for a range of temperatures (see Appendix B). The models were Doppler shifted to the velocity of AA Tau in the given year, scaled by the telluric transmittance, convolved to the resolution of the data, and scaled to fit the residual until the best-fit model was found that minimized the χ^2 value. The molecular parameters, including line positions, Einstein-As, and intrinsic line strengths are from the 2012 update to the HITRAN molecular database (Rothman et al. 2013).

4.2.1. Challenges of Disk Modeling. Fitting the observed spectra proved difficult due to the "forest" of water features present throughout the 3 μm region. This

problem was exacerbated by the presence of narrow absorption features on top of broad emission features, an issue independent of the already abundant water features. The result is spectra of heavily blended lines that prevent isolation of a substantial amount of individual transitions. Many water features are comprised of a blend of multiple lines of water with a range in lower state energies, making them un-diagnostic to changing temperature. These features were not used when determining the rotational temperature.

The issues with the excitation structure of water in the infrared are not unique to AA Tau or even the 3 μm region. Banzatti et al. (2012) note in their analysis of mid-infrared water in EX Lupi that it was impossible to get a good fit over their wide spectral range with a single temperature and column density. Salyk et al. (2011) attempted to derive average gas properties for 48 T Tauri systems, but they noted that it is impossible to reproduce entirely their observations from 10 – 35 μm and that the outcome varied if they used different spectral ranges. Carr & Najita (2008, 2011) focused on fitting lines in the smaller range of 12 – 16 μm but despite reasonable fits over that narrow range, arrived at over-predictions at longer wavelengths. Additionally, Carr & Najita (2011) note that to fit their water observations a "fit by eye" method was invoked as calculating a χ^2 from the difference of the model and observed spectrum fails to work well over their wavelength interval.

An obvious caveat to these reported difficulties is the ubiquitous approximations used in modeling water spectra. As is the case here and in those cases discussed above, the observed gas is assumed to be in LTE. In LTE, the population of the excited levels is taken to follow the Boltzmann distribution. This LTE assumption is coupled with single-slab disk models that do not account for additional disk geometries (e.g., flaring),

structure, or temperature/column-density profiles. A non-LTE model that performs line radiative transfer and accounts for the physical structure of disks would be required to rectify many of the short comings of current water modeling. However, while such a method has been explored to some degree (e.g., Pavlyuchenkov et al. 2007 or Meijerink et al. 2009), the lack of information concerning collision data prevents viable application of it to infrared water (van der Tak 2011).

To tackle these problems, emission and absorption were considered separately, with an emission model first fit and removed from the observed spectra before then fitting an absorption model, as described below. Due to correlations between models and data being comparable for a range of temperatures and dependent on which transitions were used in the analysis, in addition to systemic errors that are difficult to quantify due to the use of an LTE model, it is not straightforward to define uncertainties in some of our results, particularly for temperatures and the emission models (see Sections 4.2.2., 4.2.3., and 4.2.4.) (Salyk et al. 2009). We also note that there are many features that appear to be real (they are reproduced in the data acquired in both years) that are not in the water database, are not attributed to other species expected in that spectral region (like HCN, C_2H_2), and remain unidentified.

4.2.2. Pre-Dimming Emission in AA Tau. Figure 4.1 shows sample regions of the normalized 3 μm spectra of AA Tau taken in Feb. 2010, plotting telluric subtracted residuals alongside telluric and photospheric models and best fit water (emission and absorption) and OH (absorption only) models. The profile shapes consist of broad water emission features with underlying, narrow absorption features of both water and OH. The elimination of much of the water emission features due to the absorption features

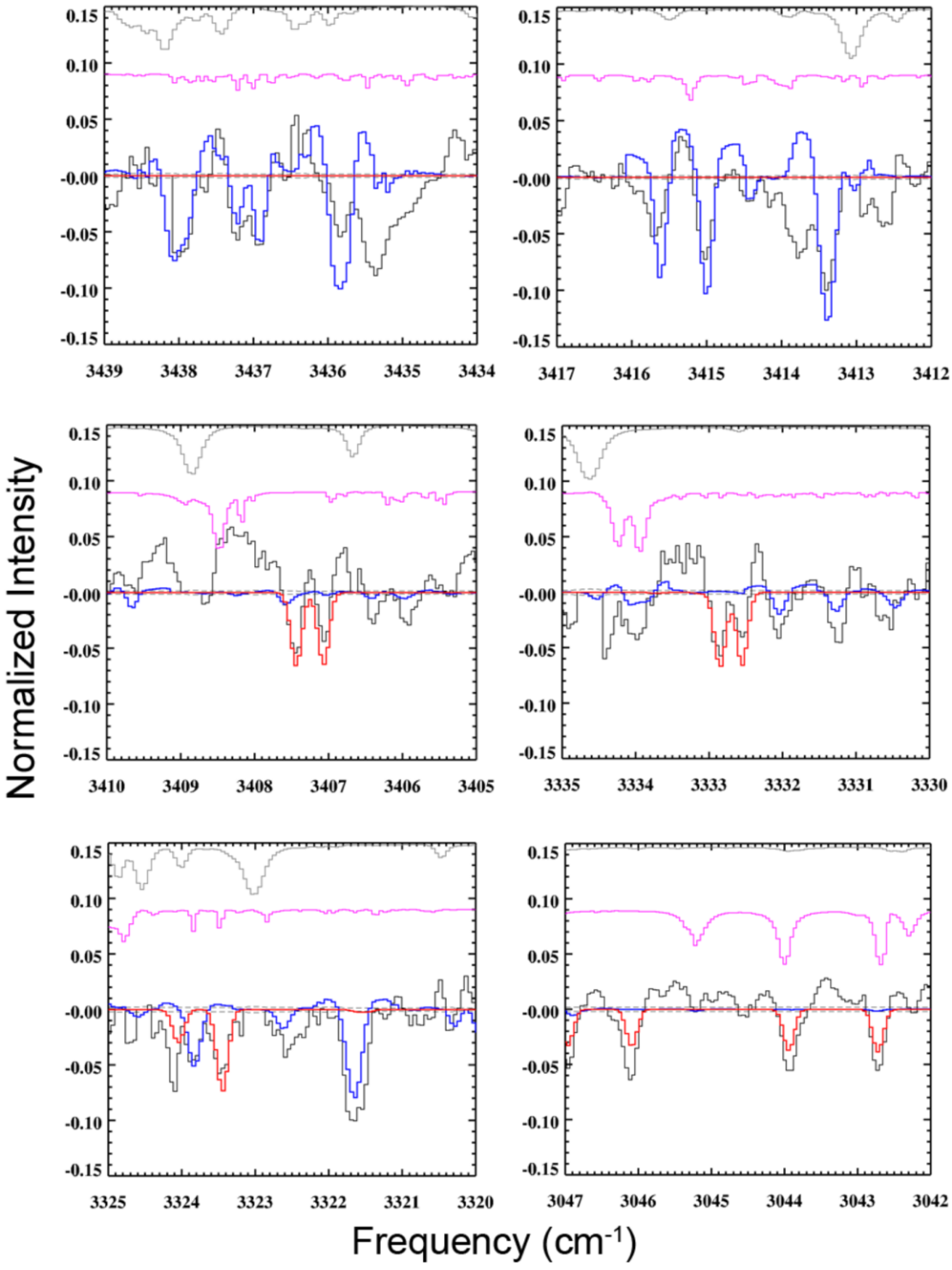

Figure 4.1. Sample spectra of AA Tau from Feb 2010. Overplotted are the telluric model in grey (top), photospheric model in purple (middle), telluric subtracted residual in black, dashed line error envelope, water model in blue, and OH model in red. Regions of less than 40% transmittance were eliminated.

coupled with the extensive blending of water lines (see Section 4.2.1) and the superposition of absorption features, permit only the outer wings of each emission line to be fit. This resulted in non-unique best fits when fitting emission models. To address this, we turned in part to the literature for constraints on the physical parameters needed to generate the emission models, as well as constraining said parameters as much as possible with what could be afforded to us from the wings of the features.

The first step toward constructing a water emission model was to determine the water emitting region within the disk, which requires an estimate of both the inner and outer emitting radii. The center of the emission feature is dominated by the lower velocity material in the outer emitting region. As noted above, the superposition of absorption features preclude fitting of emission models to the emission line centers. Therefore, a "dummy" outer radius of 0.5 AU was used based on the outer emitting radii and emitting areas reported for similar objects in the literature (see for example measurements by Salyk et al. 2008, Pontoppidan et al. 2011, and Brown et al. 2013, and the protoplanetary disk model of Walsh et al. 2015). This outer radius was used in conjunction with a variable inner radius to fit models (see Section 3 and Appendix B) to the emission wings to determine a best fit "width" and inner emitting radius. For AA Tau, we determined an inner emitting radius of ~0.02 AU and a corresponding emitting area of ~0.8 AU^2. Changing the outer radius to a value higher than 0.5 AU takes the emitting area above the upper limits reported by others for similar objects. Adopting the range of values observed for emitting radii of others (see Table 4.2 below; Doppmann et al. 2011, Salyk et al. 2008, Brown et al. 2013) only produces an ~±20% change in the resulting emission column density.

Once the emitting region was constrained, a simple, LTE, slab model of a protoplanetary disk (see Section 3 and Appendix B) was used to generate the unique, double peaked emission line profile. Spectral models were calculated (see Appendix B) with an assumed rotational temperature of 1000 K based on temperatures reported in the literature for emitting regions akin to what was used here (Salyk et al. 2008, Carr & Najita 2011, Doppmann et al. 2011). These models were convolved to the calculated line shape (see Appendix B), and were then scaled to the observed wings of the water emission features such that the total area under the curve of the selected regions of the spectra matched the model. The measured equivalent widths (W_λ) were then relate to the total column density as:

$$N_{tot} = \frac{W_\lambda}{(8.853 * 10^{-13}) f} \frac{Q_{tot}}{g_{low} e^{-hcE_{low}/kT_{rot}}} \tag{4.3}$$

where f is the oscillator strength of the line, E_{low} is the lower state energy, g_{low} is the lower state degeneracy, T_{rot} is the rotational temperature, and Q_{tot} is the total partition function at the rotational temperature of the gas. h, c, and k are Planck's constant, the speed of light, and Boltzmann's constant respectively.

For the case of emission, the column density must be multiplied by a beam dilution term (e.g. Brittain et al. 2005):

$$N_{tot,emit} = N_{tot} \frac{e^{A_L/1.086}}{A_{emit}}. \tag{4.4}$$

where A_{emit} is the area subtended by the emitting molecule and A_L is the extinction in the L band due to interstellar/circumstellar dust along the line of sight, which prior to the dimming event was not significant. This beam dilution is only necessary when the emission does not fill the beam, as is the case when the emitting region corresponds to an

angle much smaller than the observing slit width. A simple least chi squared analysis was done to fit the emission model, despite only having the wings of unblended features to utilize for the goodness of fit calculation. The column density for water emission in 2010 was 1.7 x 10^{20} cm^{-2}. We also note that while OH clearly appears in absorption, a single temperature, slab model could not reproduce any OH emission features. While there is what looks like OH emission in the 3044 cm^{-1} region (see Figure 4.1), lower J lines do not show strong evidence for emission. This may be that there is not a significant amount of OH emission for us to be able to detect, or that the extensive blending present in the spectra of AA Tau prevent us from being able to isolate any emission uniquely OH in origin.

4.2.3. Pre-Dimming Absorption in AA Tau. To fit the absorption lines, the best-fit water emission model was subtracted from the data to isolate the absorption features. In contrast to the emission models, the absorption models were convolved to a Gaussian shape as opposed to the double peaked features that typify the emission of highly inclined protoplanetary disks.

To check whether the column densities of the absorption lines were derived from optically thin lines, and therefore no correction for optical depth was necessary, we estimated the maximum optical depth of the observed transitions. Given the oscillator strength and total column density above (equations 4.3), the optical depth can be calculated as follows:

$$\tau = \frac{N_{tot} N_{J'',rel} f}{(6.68 * 10^{6}) \nu W_{\text{int}}}. \qquad (4.5)$$

In Equation 4.3, W_{int} is the intrinsic line width given by:

$$W_{\text{int}} = \sqrt{\frac{2kT_{rot}}{m}} \tag{4.6}$$

where m is the mass of the molecule in question. A value for τ on the order of 1 or <<1 is sufficient to be considered optically thin, and in the case of our observations, a maximum τ of ~1.5 was calculated. In total, only 9 in approximately 2500 transitions within our observed spectral range gave values greater than 1, with the rest being <<1, which lead us to reasonably consider our observations optically thin. See Appendix B for a detailed discussion of the modeling.

Water and OH were fit, varying the temperature and calculating the best fit in a similar fashion to water emission above. Our best fits for water and OH absorption respectively arrive at temperatures of 1640 K and 1620 K, with corresponding total column densities of $1.3 \pm 0.6 \times 10^{18}$ cm^{-2} and $4.2 \pm 0.4 \times 10^{17}$ cm^{-2}. Figure 4.1 shows a sample of the observed 2010 spectra with telluric, photospheric, water, and OH models overplotted.

4.2.4. Post-Dimming AA Tau. A cursory examination of the 2014 emission features showed only minor differences between the two epochs (see Figure 4.2) such that, for the purpose of our analysis, we assumed the same emission model. However, both the water and OH absorption features were significantly weaker in 2014. To analyze the changes in the absorption features, we adopted the same emission model used to analyze the 2010 spectrum and subtracted it from the 2014 spectrum.

As shown in Figure 4.2, OH absorption was significantly weaker in 2014. The equivalent width and column density dropped by about a factor of three, with a resulting column density of $1.5 \pm 0.7 \times 10^{17}$ cm^{-2}. In particular, the lower right panel of Figure 4.2 shows that the modeled, disk component of OH is predicted to be within the 1-sigma

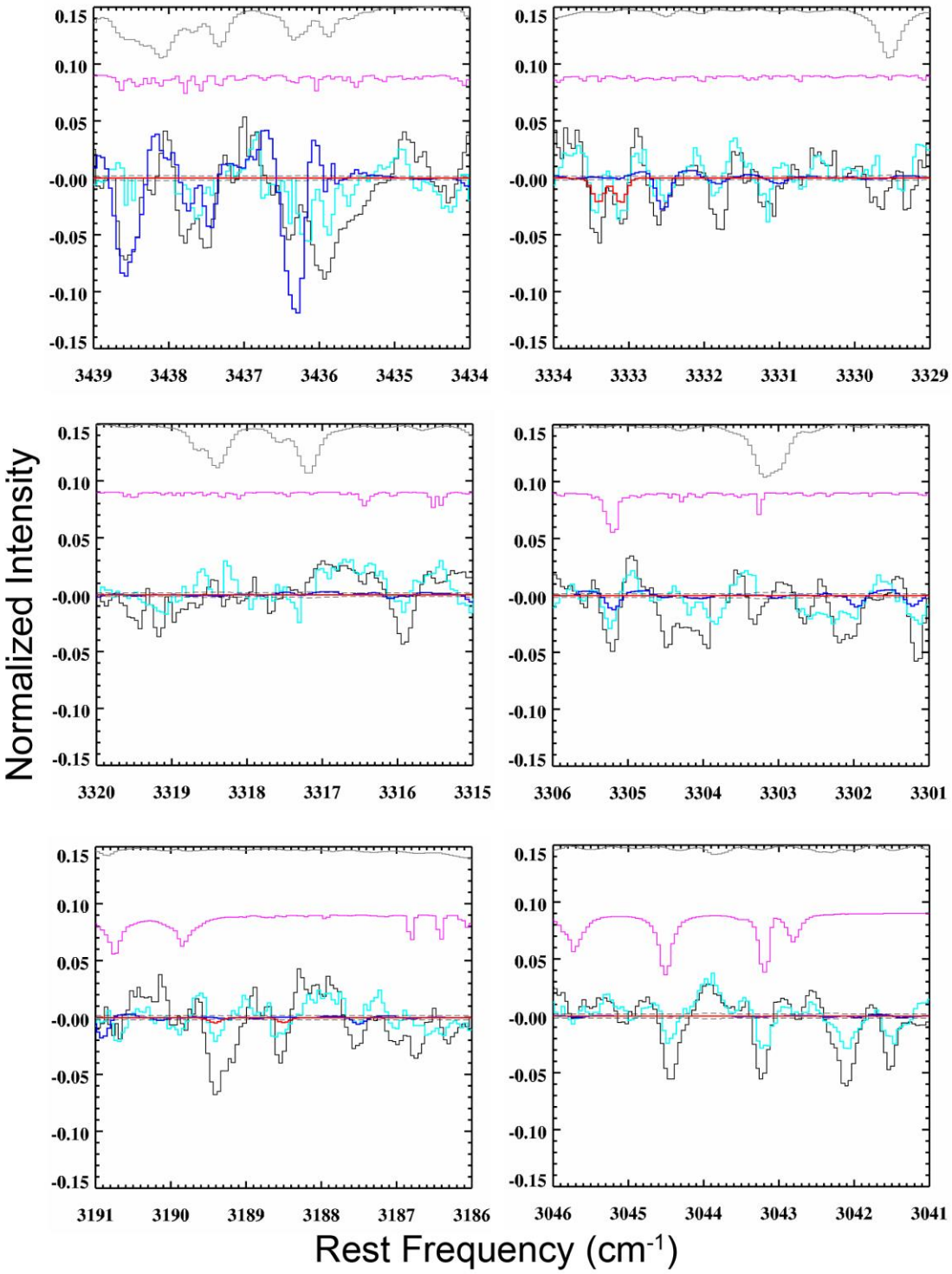

Figure 4.2. Overlapping spectra from 2014 (cyan) and 2010 (black), with the 2014 telluric model in gray (top), 2010 photospheric model in purple (middle), and dashed line indicating the 2014 error envelope. The red is the 2014 OH model, and the blue is a combination of the 2010 H_2O absorption model (with column density reduced by a factor ~3), 2010 H_2O emission model, and the 6 km s^{-1}, Doppler shifted 2014 H_2O absorption model. The spectra and models have been Doppler shifted to the rest frame and regions of less than 40% transmittance have been eliminated. Note the overall reduction in equivalent of water and OH between 2010 and 2014.

error envelope, suggesting those features are primarily photospheric in nature. When attempting to fit temperatures of 500 K – 2000 K, anything at or above ~1000 K gave approximately the same column density, all falling within the uncertainty reported above. The equivalent widths of water features were also significantly weaker in 2014 compared to 2010. As previously discussed at the beginning of Section 4.2 above and illustrated in Figure 4.3, water appears to be composed of two different components, one of which is at a ~6 km s^{-1} redshift.

Interestingly, we were not the only ones to observe a redshift in the spectra of AA Tau after the dimming event. Zhang et al. (2015) observed CO features during eight different epochs between November 2003 and September 2014. They noted that their observed CO absorption features were significantly deeper after the dimming event. The difference between spectra of two years (specifically December 2004 and January 2013) were taken so the additional absorption that appeared could be analyzed. The observed absorption centers were found to have a clear and constant redshift of ~6 km s^{-1}, matching what we observed in water. A temperature of 500 K was used to fit the extra absorption by Zhang et al. (2015) and they presented a possible scenario where a magnetic field instability lifted disk material to large heights (see Section 4.3.3 for additional discussion of this scenario).

To try analyze our 2014 water observations, we adopted a similar methodology to Zhang et al. (2015). To isolate the redshifted water component, the 2010 water absorption model was taken with its column density reduced by a factor of ~2.9 (assuming an unchanged water-to-OH ratio between 2010 and 2014) and subtracted from the 2014 spectra. With the scaled 2010 absorption component removed, an assumed 500

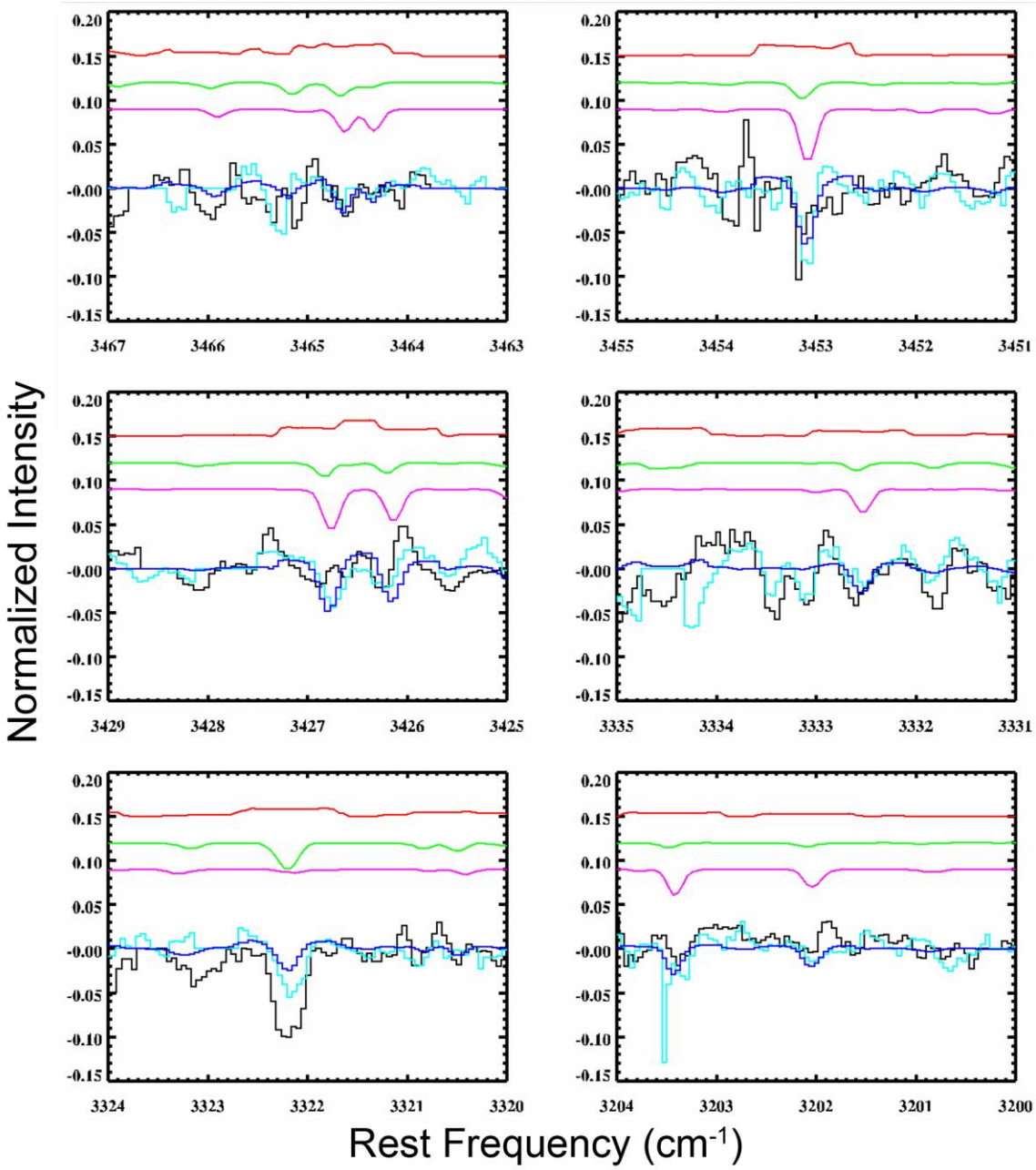

Figure 4.3. Overlapping spectra of AA Tau from Sept 2010 (black) and 2014 (cyan). Plotted are the 2010 water emission model (red), the 2010 water absorption model reduced by a factor of 2.9 (green), and the 2014, Doppler shifted water absorption model (purple). Overplotted on the sample spectra is the combination of the three water models (blue). The spectra and models have been Doppler shifted to the rest frame and regions of less than 40% transmittance were eliminated.

K water absorption model was fit to the remaining residual, arriving at a column density of $2.3 \pm 0.3 \times 10^{19}$ cm^{-2} for the Doppler shifted component of the water absorption, a significant increase from 2010. A temperature of 500 K was chosen to put a limit on how much water could be cospatial with the CO observed by Zhang et al. (2015), a reasonable assumption given the similar Doppler shifts we observed.

4.3. DISCUSSION

We detected H_2O and OH emission and absorption near 3 μm with NIRSPEC, originating from the protoplanetary disk of AA Tau in 2010 and 2014. The wings of the emission features suggest an inner emitting radius of ~0.02 AU, with an assumed temperature of ~1000 K (see Section 4.2.2), suggesting inner disk emission from the hot disk atmosphere. The warm water and OH best-fit temperatures of 1640 K and 1620 K respectively in 2010 suggest that the sampled absorbing material must be dominated by gas in the hot inner disk region as well.

4.3.1. Other Objects. How do our values compare with what has been found by others and would be expected from astrochemical modeling of protoplanetary disks? Table 4.2 summarizes water and OH observations for a few sources, similar to AA Tau and based on observations performed in the same spectral region as presented here. Our values fall within the ranges observed by others. While our assumed emitting region for water is on the high end of values, it is still within upper limits found for the emitting regions of water for similar objects (e.g. AS 205N's 0.8 AU^2 Pontoppidan et al. 2011). Our water emission column density appears to be close to that of the V1331 Cyg column density (within ~1 order of magnitude). Our water column densities in absorption are

Table 4.2. Near IR Observations of AA Tau & Similar Sources

Molecule	Source	Column Density (cm^{-2})	Temperature (K)	Emitting Region (AU)	Emitting Area (AU^2)
Water	V1331 Cyg	2×10^{21} [a]	1500[a]	0.03 – 0.09[a]	0.023[a]
	DR Tau	8×10^{17} [b]	900 – 1200[b]	0.056 – 0.38[c]	0.44[c]
	AS 205A	6×10^{17} [b]	900 – 1100[b]	-	0.4[b]
	AA Tau 2010 (emission)	1.7×10^{20}	1000	0.02 – 0.5	0.78
	AA Tau 2010 (absorption)	1.3×10^{18}	1640	N/A	N/A
	AA Tau 2014 (absorption)	2.3×10^{19}	500	N/A	N/A
OH	V1331 Cyg	1×10^{20} [a]	1500[a]	-	~0.046[a]
	DR Tau	-	$T \geq 900$[b]	-	-
	AS 205A	-	$T \geq 900$[b]	-	-
	AA Tau 2010 (absorption)	4.2×10^{17}	1620	N/A	N/A
	AA Tau 2014 (absorption)	1.5×10^{17}	1000	N/A	N/A

NOTE. - (a) Doppmann et al. 2011. (b) Salyk et al. 2008. (c) Brown et al. 2013.

higher than what has been reported in DR Tau and AS 205A. The temperatures we found for water and OH appear to agree reasonably well with those reported for V1331 Cyg, while water appears to be warmer than that of DR Tau and AS 205A.

Water and OH were studied within AA Tau in the mid-infrared by Carr and Najita (2008, 2011). Carr and Najita (2011) found an emitting temperature of 575 ± 50 K, column density of $7.8 \pm 2.0 \times 10^{17}$ cm^{-2}, and emitting radius of 0.85 ± 0.12 AU for water. While their observations sampled disk material further out in the disk (as suggested by the lower temperature and consistent with the longer wavelengths), it is interesting to note they only observed water in emission and not also in absorption.

4.3.2. Disk Modeling. Recent disk modeling work by Walsh et al. (2015) suggests a vertical column density within 0.1 – 1.0 AU for water on the order of 10^{22}

cm^{-1}, with OH column densities on the order of 10^{16} cm^{-1}. However, those values are not directly comparable to ours as Walsh et al. (2015) reports vertical column densities while absorption line studies like those found here or in Gibb & Horne (2013) measure column densities through the disk at high inclination angles. Disk absorption studies depend sensitively on the height above the midplane sampled by the observations which necessitates additional modeling of temperature profiles and column densities as a function of inclination for nearly edge-on sources. This may lead to a better understanding of why organic molecules such as CH_4 are not observed in other nearly edge-on sources (e.g. DG Tau B) (Gibb & Horne 2013). Additionally, total column densities through the disk are given while for typical observations water and OH would become be optically thick for such high column densities. In practice, one would only be sampling the disk surface, rather than the total vertical column density.

4.3.3. Dimming Event. For at least 24 years from 1987 to 2010, AA Tau remained at a nearly constant maximum brightness level (V ~ 12.4-12.6 mag) (Grankin et al. 2007). Bouvier et al. (2013) reported that AA Tau suddenly dimmed in the visible by two magnitudes in 2011 and has remained in the dim state through at least 2015 (Schneider et al. 2015, Zhang et al. 2015). While the exact nature of this dimming event is still a matter of debate, much can be said about AA Tau's current state.

The dimming of AA Tau was verified to be restricted to it alone in two ways (Bouvier et al. 2013): 1) by comparing CCD images taken at Calar Alto on Dec. 2011 with the SDSS9 catalog release taken between Dec. 2009 and July 2011 (Ahn et al. 2012) where the three field stars nearest to AA Tau showed no luminosity variation; and 2) by looking at the bright and deep state luminosity of AA Tau's jet, as measured by the [OI]

line flux, which remained unchanged. Therefore, it was concluded that an intervening cloud was not the cause of the dimming. A visual extinction increase of 3-4 mag was suggested by the JHK color changes compared with the bright state (Bouvier et al. 1999, Bouvier et al. 2013). In surprising contrast to other observations of disk variability (e.g. Sitko et al. 2012), AA Tau's dimming was not accompanied by any significant change in the mass accretion rate onto the central star based on H_α and H_β line fluxes and the range of mass accretion rates derived for AA Tau in the bright state (Valenti et al. 1993, Bouvier et al. 1999, Donati et al. 2010, Bouvier et al. 2013). Bouvier et al. (2013) also found that as direct photons are being absorbed by the dusty disk along the line of sight, scattered light dominates the system's optical flux at minimum brightness, making it bluer. This behavior is in fact typical of UX Ori-type variables and results from obscuration by circumstellar dust (e.g. Grinin et al. 1991, Herbst et al. 1994).

A density perturbation, possibly the result of a low-mass companion or planetary embryo, located at a distance of $\geq$ 7.7 AU from the central star was invoked as a possible explanation for the dimming by Bouvier et al. (2013). Zhang et al. (2015) explored this notion, and the enhanced ^{12}CO and ^{13}CO absorption observed, their observed CO emission and M-band continuum arising from very small regions (R < 0.5 AU), and a constant observed redshift of ~6 km s^{-1} for CO absorption compared to the CO emission at stellar velocities would suggest that any such perturbation rotating at Keplerian speeds must lie beyond >8.4 AU and would have an orbital period of at least 27 years. This orbital period is longer than the total time span of AA Tau observations, suggesting this is the first time the perturbation would have been observable.

Zhang et al. (2015) also presents a possible scenario where a magnetic field

instability lifted disk material to large heights which will lead to a possible accretion outburst involving the transport of this gas and dust inward, leading to the possibility that AA Tau is a pre-EXor object (Zhu et al. 2010). This suggestion is backed up by the observed Herbig-Haro objects of Cox et al. (2013), which are usually associated with elevated accretion activity in young stars, and the observed redshift of the CO absorption suggesting propagation inward (Reipurth & Bally 2001, Zhang et al. 2015). Zhang et al. (2015) places this excess dust and gas at ≤ 10 AU based on the warm temperature of the absorbing gas (~500 K). In contrast to Zhang et al. (2015), Schneider et al. (2015) acquired x-ray observations of AA Tau that are incompatible with the mid-IR CO, finding an increase in CO column density less than a factor of 1.6, which gives a column density a factor 1.5 less than that of Zhang et al.

So how do our observations of AA Tau in the NIR fit with those done in the FUV, optical, and mid-IR before and after the dimming event? Zhang et al. (2015) observed CO with a Doppler shift with respect to AA Tau of ~-6 km s^{-1} with a temperature of ~500 K. The CO Doppler shift is consistent with what we observed for water absorption in 2014. In turn, we assumed a 500 K as the temperature for the 2014 water absorption (see Section 4.2.4) to test how much of the proposed infalling material could be due to water. Interestingly, a reduction in equivalent width was observed here between 2010 and 2014 for both OH and water, but the redshifted water component shows a large increase in water column density compared to 2010. In contrast, enhanced absorption for CO was observed by both Zhang et al. (2015) and Schneider et al. (2015). The observed Doppler shift in 2014 water absorption lends credence to the scenario put forward by Zhang et al. (2015) of magnetic field instability lifted disk material, and while we suddenly find AA

Tau to be depleted of OH since the dimming event began, water appears to have increased in column density despite a drop in equivalent width.

What sort of scenario then can be invoked to reconcile these discrepancies with our observations and the Zhang et al. (2015) scenario? If a magnetic field instability has lifted disk material beyond 7 – 10 AU as suggested, this should be beyond the water snow line where it would be reasonable to expect most water to be frozen out and settled into the midplane. This is evidenced by the modeling of Walsh et al. (2015) where water gas abundances are shown to drop off dramatically beyond ~1 AU. However, the uplifted material could have "dredged up" water ice that has since warmed and sublimated into a gas again, explaining the column density increase of the Doppler shifted water. At the same time, Walsh et al. (2015) shows that CO would stay in the gas phase out to at least ~10 AU. Additionally, while Zhang et al. (2015) primarily viewed low- and mid-energy transitions ($J_{low} \leq 13$) which would be stronger in a cooler gas (the 500 K gas reported as opposed to the ~1600 K gas discussed in our 2010 observations), we fit higher energy water lines which would result in an increase in column density despite a drop in equivalent width based on the line strength at that temperature.

If we hypothesize that water is mixed with CO, we determine a H_2O/CO ratio of 7.3×10^{-4}. Based on disk modeling, one would expect a H_2O/CO ratio on the order of 10^{-6}, quite a bit less than our proposed scenario (Walsh et al. 2010). However, water is normally frozen out beyond about ~1-3 AU and heavily depleted from the gas phase so this ratio could be enhanced by "dredging up" water ice by a magnetic instability. We also note however that the "lifted disk material" scenario is still highly speculative, and Zhang et al. (2015) commented that it will take a few years of observations, noting any

changes to accretion rate or subsequent outburst duration, before being able to draw any firm conclusions. However, studies like this and those of Zhang et al. (2015) and Schneider et al. (2015) over the coming years will continue to shed light on what will possibly be new and interesting insight into disk dynamics.

5. CLOSING REMARKS

As stated in Section 1, one of the primary motivators for studying water in protoplanetary disks is astrobiological in nature, to better understand the origin of life by shedding light on the origin of Earth itself. When considering life as we know it, water is of paramount importance and was the primary target of both our DR Tau and AA Tau observations. Our current understanding of biology shows that life requires a solvent to perform an active, diverse, and flexible role, and as it stands right now, water is the only common liquid that is capable of this (Ball 2001).

If water is so important to life on Earth, an obvious question to understanding our origins is how that water got to Earth. This is a topic of much debate to which there are three likely possibilities (Tornow et al. 2014): 1) it was there when planet Earth formed, accumulated from the Solar Nebula; 2) it arrived soon after Earth formed, delivered by water-containing, rocky asteroids; and 3) it arrived later on from icy comets. The truth of the matter is likely some combination of the three. Regardless of the debate, this illustrates the importance of studying water in protoplanetary disks. As illustrated in the observations here and of others, protoplanetary disks around T Tauri stars clearly contain water and are reasonable analogs for our early solar system.

5.1. DISK/COMET CONNECTION

Comets, along with everything else in the Solar system, were birthed from the Solar Nebula and the protoplanetary disk that once surrounded our Sun, and it is posited that comets present the final midplane composition of said disk (Mumma & Charnley

2011). Many comets reveal spectral signatures of crystalline silicates that would require high-temperature processing, suggesting that radial and vertical transport mechanisms were important to the overall final compositions (Mumma & Charnley 2011; Caselli & Ceaccarelli 2012). Together, this suggests that comets may give us insight into the formation of our own solar system, and by extension, protoplanetary disks and planet formation at large.

However, it is uncertain whether the chemical similarities between comets and protostellar environments signifies the inheritance of materials or a coincidence caused by astrophysical conditions guiding chemistry along similar pathways (Drozdovskaya et al. 2016). One hurdle to overcome this and to fully understand the disk/comet connection is trying to place where comets would have been formed within the protosolar disk. Originally, Jupiter-family comets were thought to have formed in the Kuiper Belt region (R > 30 AU) and Oort cloud comets formed in the giant planets' region (5-30 AU), with the expectation that radial variations in the conditions of the protoplanetary disk would manifest as distinct compositions for comets in those two regions (Mumma, Weissman, & Stern 1993; Boss 1998). However, the advent of the Nice model and its migration of Saturn into 1:2 orbital resonance with Jupiter triggered the disruption of outer disk planetesimals and a primordial asteroid belt (Gomes et al. 2005; Morbidelli et al. 2005; Tsiganis et al. 2005; O'Brien, Morbidelli, & Bottke 2006). As result, outer disk and giant-planet zone objects would have been deposited in both the Kuiper Belt and Oort Cloud.

Through a combination of gas-phase and ice-phase chemistry, a comet-like composition of simple and complex volatiles has been found in protostellar envelopes,

and it should be clear by now that these simple volatiles can survive the formation and environment of protoplanetary disks to end up in comets (Herbst & van Dishoeck 2009, Visser et al. 2011). A'Hearn et al. (2012) suggests that successive perihelion passages is an unlikely cause of the observed variation in abundances of volatile species such as H_2O, CO_2, and CO among both classes of comets, going on to posit that both classes were formed between the CO_2 and CO snow lines of our solar system. This further illustrates the importance of an understanding of the disk environment and the processes that may have affected material in the protoplanetary disk and how that can shed light on where these comets had to have been to arrive in their final state. Gibb & Horne (2013) touched on this with their CH_4 observations for the disk of GV Tau N, with results within the range of values observed in comets, HCN/CH_4 ~10%-50% and HCN/CH_4 ~7%-35% (Mumma & Charnley 2011; Gibb et al. 2012). Disk modeling also aids in understanding the disk/comet relationship, with modeled volatile contributions relative to water ice being in close agreement (within a factor of 2) to observed ranges for cometary volatiles (Mumma & Charnley 2011; Drozdovskaya et al. 2016). Further observations such as those found here may yet shed additional light on cometary origins through furthering the understanding of protoplanetary disk environments, justifying such a comparison.

5.2. DISKS IN THE AGE OF ALMA

Since protoplanetary disk structure consists of a gradient of temperatures and composition, there is a necessity to work in a variety of spectral ranges (as discussed in Section 1). ALMA has provided invaluable data of protostars and protoplanetary disks in the millimeter regime. Tying back into astrobiological motivations and comets, recent

ALMA observations explored complex organic molecules (CH_3CN, HCN, HC_3N), finding abundance ratios of those N-bearing organics in the gas-phase similar to comets (Öberg et al. 2015). Additionally, the simplest sugar and an important intermediate in the path toward more complex molecules, glycolaldehyde ($HCOCH_2OH$), was observed for the first time around a solar-type young star using ALMA (Joergensen et al. 2012). Thirteen transitions of glycolaldehyde were detected around a Class 0 protostellar binary IRAS 16293-2422, with a reported origin in warm (200-300 K) gas, and glycolaldehyde serves as an important step in understanding the full chemistry of biologically relevant molecules in these objects (Joergensen et al. 2012).

ALMA findings have begun pushing the onset of planetesimal formation much earlier along the star-disk evolutionary sequence (Drozdovskaya et al. 2016). The Class I-II protostar HL Tau exhibits ring structures in the disk, tied to several planets of ~0.2 M_J in mass clearing gaps in the dust (ALMA Partnership et al. 2015, Dipierro et al. 2015b; Pinte et al. 2016; Dong, Zhu, & Whitney 2015). Alternatively, enhanced dust growth leads to a change in opacity in the emitting dust, a notion aided by sintering close to the snowlines of the volatiles (Zhang, Blake, & Bergin 2015; Okuzumi et al. 2016).

Insight into the dynamics of disk dust and gas has also been provided by ALMA. Zapata et al. (2013) observed infalling gas associated with fast and turbulent regions close to IRAS 16293-2422B as indicated by an inverse P-Cygni profile of observed $H^{13}CN$, $HC^{15}N$, and CH_3OH absorption and emission. Additional gas dynamics were studied using ALMA of the young star HD 142527, using HCO^+ which was shown to trace filaments of gas bridging the large gap present in the disk, with speculation that the gap-crossing accretion flow may be material straddling the putative protoplanet also

responsible for clearing the gap (Casassus et al. 2013). Around R Sculptoris, an asymptotic giant branch star, a previously unknown spiral structure was resolved by ALMA and observations of the object and other objects like it suggest they are major contributors to the galaxy's reservoir of star, planet, and life forming material (Maercker et al. 2012).

While ALMA has made great strides in our understanding of star formation and protoplanetary disks and can provide previously unobtainable spatial resolution, it cannot do everything on its own. ALMA's spectral range covers 0.3 mm to 3.6 mm (300 μm to 3600 μm)[3], values much larger than the spectral ranges shown in Sections 3 and 4. This for example precludes ALMA from being able to do work with vibration transitions of water which requires work in frequencies not covered by ALMA. This illustrates importance of studying protoplanetary disks with a number of different instruments that cover a large spectral range, such as NIRSPEC.

5.3. GOING FORWARD

There is much work that can still be done going forward. Additional near infrared observations of T Tauri stars akin to DR Tau with suitable time on source to facilitate the use of SA will hopefully find SA signals for organic volatiles such as HCN or CH_4 to better understand the spatial distributions of these molecules in the inner disk environment. Future work with DR Tau could also include modeling additional factors such as a disk wind, fully exploring the parameter space, and exploring constraints on OH emission which was detected but for which we do not detect an SA signal.

[3] https://science.nrao.edu/facilities/alma/summary

While 2010 and 2014 observations of AA Tau were shown (see Section 4), we also have 2009 and 2011 observations waiting to be analyzed. Having observations spanning five years could give an interesting look into the variability of AA Tau and perhaps shed additional light into events leading up to the dimming event in 2011. In addition, a more rigorous modeling of the observed AA Tau spectra would aid its analysis, particularly addressing the many shortcomings in disk modeling methodology of the community at large such as assuming LTE or using single temperature models.

In conclusion for DR Tau, our spectro-astrometric analysis, in addition to spectroscopic modeling and protoplanetary disk chemical modeling, suggest a scenario in which we observed hot water emission from the disk atmosphere above the inner, terrestrial planet region of a protoplanetary disk. AA Tau presented a much more complicated picture where AA Tau's nearly edge on geometry provides both emission and absorption in the observed spectra. Through spectroscopic analysis and chemical modeling of two viewing dates for AA Tau (2010 and 2014), we have a scenario that suggests we observed hot water emission from the disk atmosphere above the inner most disk regions while also observing hot OH and water absorption presumably from a similar radial region within the disk. AA Tau also went through a dimming event in 2011, which resulted in a drop in column densities for both OH and water between 2010 and 2014 and the introduction of a new, Doppler shifted water component with enhanced column density compared to 2010. Taken together, they broaden our understanding of water in protostellar environments, allowing us to further assemble an understanding of what the protosolar environment might have been like.

APPENDIX A.

SPECTRO-ASTROMETRY

Astronomers' limitations on the ability to understand astronomical phenomena are based heavily on the need for better angular resolution. While advancements in adaptive optics and interferometers have made great strides in tackling this issue, the technique of Spectro-Astrometry (SA) allows for the studying of spatial structure well below the limit on resolution set by the seeing disk size or the diffraction limit. Combining the techniques of spectroscopy and astrometry, SA is the astrometric measurement and analysis of spectrally dispersed images, and it relies on the fact that the relative position of a source at two or more wavelengths can be measured to an accuracy limited only by photon statistics if the measurements are simultaneous (Whelan & Garcia 2008). The concept was introduced in the 1980s as "Differential Speckle Interferometry" or "Chromatic Position Difference" (Beckers 1982) and demonstrated by detecting close binaries (Sorokin & Tokovinin 1985).

The concept behind SA is to measure the relative position of the source as a function of wavelength by centroiding or profile-fitting in the spatial direction and requires no special instrumentation (Bailey 1998). This results in a "position spectrum" with structure arising from any spectral feature that is displaced from the centroid of the continuum source, that is any structure that is not perfectly symmetric about the centroidal source or whose displacement from the source varies with wavelength (Brannigan et al. 2005). Possible effects that could generate such structure include a binary star with a spectral line present in only one component, outflowing jets, or hot gas-phase emission for the inner region of a protoplanetary disk.

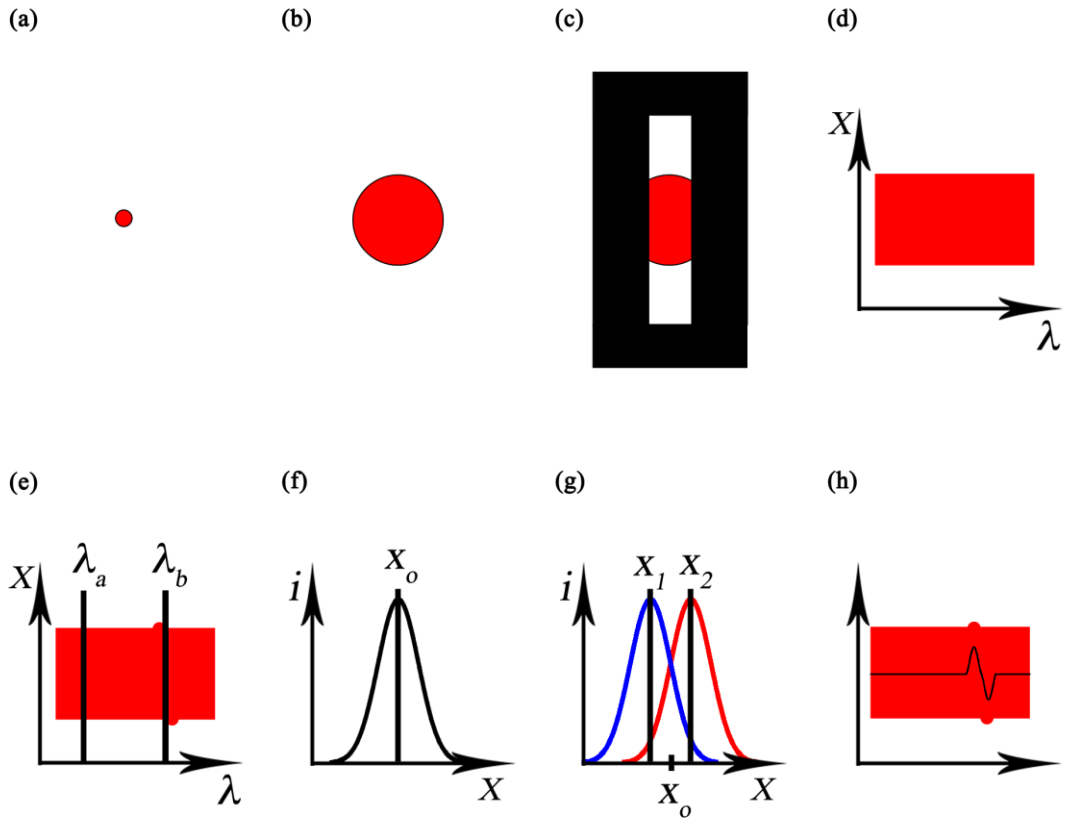

Figure A.1. (a) A point source to be observed. (b) The diffracted image of the source. (c) The image as it would appear aligned with the slit of the telescope. (d) The image dispersed onto the detector. (e) Two wavelengths, λ_a marking continuum and λ_b marking an emission feature with two Doppler shifted components. (f) The Gaussian fit to the velocity channel of λ_a, where Xo denotes the "center-of-light" for that pixel. (g) The Gaussians fit to the emission feature at λ_b, showing the two Doppler shifted components and their centers differing from that of the continuum. (h) The resulting SA signal calculated for this illustrated spectrum.

A.1. MEASURING THE SA SIGNAL OF A DISK

Figure A.1 illustrates the technique of spectro-astrometry. When observing a typical protostar and disk system, it is initially (a) a point source that, when imaged by a telescope, is (b) diffracted into a blurred image. Light from the source then passes through the slit (c) and is dispersed onto the detector as a function of wavelength and

position along the slit as shown in (d). This eliminates any spatial information perpendicular to the slit. Figure A.1 (e) highlights a vertical cut in the spatial direction for a wavelength where emission is due entirely to the continuum (λ_a) and at the position of an emission feature (λ_b). A Gaussian can be fit to the profile of the diffracted image at λ_a as shown in Figure A.1 (f) and at the position of the emission feature (g). Then a SA calculation can be performed to get the resulting signal (h).

The projected velocity of gas in a rotating disk varies as a function of orbital phase and distance from the star. Regions of common projected velocity space map in loop-like structures. Thus the point spread function (PSF) of each velocity channel of a resolved emission line formed in the disk is offset from the position of the star. While the typical image quality of a PSF is limited to ~1.2 λ/D, approximately half a pixel in the near infrared, SA observations can determine the centroid of the PSF to ~0.005–0.010 pixel given a well sampled Gaussian PSF dominated by photon noise,

$$\delta b \sim 0.4 \frac{FWHM}{SNR} \tag{A.1}$$

where b is the center of the Gaussian, $FWHM$ is the full width at half maximum power of the Gaussian, and SNR is the signal to noise ratio of the PSF (Brannigan et al. 2006).

The spatial center of the protostar was assumed to be at the peak position of the PSF in regions identified as continuum (frequencies both devoid of emission features and at good transmittance). Once the beam center was determined, the center for each pixel in frequency space was calculated. The spatial offset, the spectro-astrometric signal, was calculated by comparing the center at each pixel to the peak continuum PSF. Emission line centers were measured and compared to the continuum to test for the presence of a spatial offset. Adopting the method of Pontoppidan et al. (2008), the spatial offset was

calculated as follows:

$$X_n(v) = C\frac{\sum_i (x_i(v) - x_o)F_i(v)}{\sum_i F_i(v)}, [pixels] \quad \text{(A.2)}$$

where C is a correction factor based on the amount of flux not included in the window over which the signal was calculated and is a number of the order of unity. X_v is the spatial offset, x_i is the position of a given pixel, x_o is the centroid of the star, and F_i is the flux for pixel i at a specific wavenumber. This signal was diluted by the strength of the feature relative to the continuum. The undiluted signal was calculated as follows:

$$X_{undiluted} = X_n(1 + \frac{F_{cont}}{F_{line}}) \quad \text{(A.3)}$$

where $X_{undiluted}$ is the undiluted signal, X_v is the spatial offset, F_{cont} is the flux of the continuum, and F_{line} is the flux of the emission line.

The extent of the spatial offset depends on a number of factors. Since spatial information can only be determined along the slit, aligning the semi-major axis of the disk perpendicular to the slit will not result in a signal, while the signal intensity will be maximized when the slit is aligned on the sky parallel to the disk major axis. Similarly for disk inclination, a face on disk gives no signal and an edge on disk would maximize the signal since an observer can only see motion along the line of sight. A number of other factors also impact the calculated SA signal including the spatial extent of the emission, any asymmetries in the distribution of the emission along the slit, and the brightness of the emission relative to the continuum.

To constrain the inclination and position angle of the disk, observations must be acquired with the slit at no fewer than three different position angles to avoid aligning the slit perpendicular to the disk and have sufficient data to avoid nonunique solutions to the

spatial geometry of the disk. Artifacts from reduction and instrumental effects must also be accounted for without removing any real signal. To accomplish this, observations are also acquired with the slit aligned at 180◦ offsets to each of the 3 position angles, for a total of six sets of observations. Pairwise subtracting of the parallel and antiparallel SA signals removes reduction and instrumental errors,

$$(X_0 - X_{180})/2 \qquad \text{(A.4)}$$

where X_o is the SA signal at a given PA and X_{180} is the SA signal at a PA 180^o offset. This works because the SA signal will be vertically flipped between the pair while instrumental and reduction effects will remain unchanged. Thus those errors are subtracted off and the SA signals of the pair are effectively averaged together.

With the spatial offset calculated and reduction and instrumental effects removed, model fitting can be done to determine the spatial geometry of the disk and the spatial extent of the observed emission (see Section 3 and Appendix B).

APPENDIX B.

MODELING

The studies of both DR Tau and AA Tau required extensive modeling in order to determine rotational temperatures, line profiles, column densities, and in the case of DR Tau, SA signals. For DR Tau, in order to interpret the observed SA signal and determine the spatial extent of water emission, we modeled a protoplanetary disk, disk emission, and an artificial SA signal (see Section B.1). With AA Tau, synthetic emission and absorption spectra were fit to the data. The complicated spectrum required the fitting of overlapping emission and absorption features.

B.1. DISK EMISSION AND SPECTRO-ASTROMETRIC MODELING

Emission from a disk in Keplerian motion is expected to produce an antisymmetric SA signal, with the blue- and redshifted sides of the line offset in opposite directions. In order to interpret the observed SA signal and determine the spatial extent of emission, disk position angle, and inclination, we generated a series of a protoplanetary disk models and used them to generate synthetic SA signals that were then fit to the data. A flat, circular slab rotating with simple Keplerian motion was assumed. An adaptive mesh was used to divide the modeled disk into pieces such that any radial or angular step moved no more than a set model resolution in velocity space, with a value chosen to be approximately equal to or less than the size of a pixel in velocity units for a given observation. Each of these calculated regions was treated as its own emitting blackbody with a flux given by,

$$F = area * r^{\beta} \tag{B.1}$$

where F is the flux of a region, *area* is the emitting area of that region, r is the distance from the central protostar to the center of that region, and β determines how the flux

changes as a function of distance and with an assumed value of -3 (Mandell et al. 2012). A constant radial surface density was assumed.

The disk emitting regions were organized by velocity and binned based on the spectral resolution of the observations. A Gaussian was fit to the summed fluxes of the velocity bins and convolved to the spectral resolution of the observations to generate modeled emission features. An SA signal was calculated for the modeled feature by fitting a weighted centroid, weighted by the flux, for the velocity binned regions as follows:

$$X_{model} = \frac{\sum F * y}{\sum F} \tag{B.2}$$

where X_{model} is the modeled SA signal, F is the flux of a given region, and y is the position along the slit. Equation B.2 was applied to each velocity bin to create an artificial spatial offset that was fit to the actual offset (see Section 3 and Appendix A).

The PA of the disk was set relative to the PA of the observing slit and was varied alongside the disk inclination, inner emitting radius, and outer emitting radius to generate a series of artificial SA signals. The mass of the disk and the flux dependence on radius were held as constants. The PA and inclination have a direct impact on the SA signal, as discussed in Section 3 and Appendix A, while the radius impacts the flux term used to calculate the SA signal. In order to fit the modeled SA signals to the data, they were interpolated to the observed signals, and then they were fit to the data and a best match was determined by using a least chi-squared fit as follows:

$$\chi^2 = \sum_{i=1}^{n} \frac{(O_i - E_i)^2}{E_i} \tag{B.3}$$

where the sum was done over the range of pixels covering an observed SA signal, χ is the

goodness of fit, *O* the observed signal value at pixel *i*, and *E* is the modeled signal value at pixel *i*. The properties that generated the best fit were reported to be the physical properties of the disk and observed emission (see Section 3).

B.2. SPECTRAL LINE MODELING AND ANALYSIS

The temperatures and column densities of observed water and OH in both emission and absorption were calculated by generating synthetic models and fitting those to the observed spectra. Spectral line parameters (rest frequency, Einstein A, degeneracy, and lower stat energy) were extracted from the HITRAN database (Rothman et al. 2013). The HITRAN database also provides total partition functions for each molecule for temperatures ranging from 70 – 3000K. Lines within the desired wavelength range were extracted and the total partition function was verified through the following calculations:

$$Q = g_i \sum_{\substack{all \\ states}} g_s e^{-E_s/kT} \tag{B.4}$$

where Q is the partition function, g_i is a state independent degeneracy factor, g_s is a state dependent degeneracy factor, E_s is the state's energy, k is the Boltzmann constant, and T is temperature. The total energy is given by a sum of contributing factors:

$$E_{total} = E_{electronic} + E_{vibrational} + E_{rotational} + E_{translational} + E_{other} \tag{B.5}$$

The E_{other} term includes nuclear spin energy levels and may also be used to include interactions between the other four energies. Assuming the first terms are independent, ignoring the last term, and taking the product approximation gives:

$$Q_{total} = Q_{electronic} Q_{vibrational} Q_{rotational} Q_{translational} \tag{B.6}$$

For the work here, the electronic and translational partition functions are approximately

1. The vibrational and rotational partition functions are calculated as follows:

$$Q_{vibrational} = \prod_{\substack{vibrational \\ fundamentals}} \frac{1}{1 - e^{hcE_{vibrational}/kT}} \tag{B.7}$$

$$Q_{rotational} = d_i \sum_{\substack{all \\ rotational \\ states}} d_r e^{-E_{rotational}/kT} \tag{B.8}$$

where d_r is the degeneracy of the state with energy $E_{rotational}$.

In order to calculate column density and temperature of the observed spectra, we measured the equivalent width of the spectral lines. The equivalent width of a spectral line is a measure of the area of the line on a plot of intensity versus wavelength, and is given by:

$$W_\lambda = \int (1 - F_\lambda / F_0) d\lambda \tag{B.9}$$

Here, F_0 represents the continuum intensity on either side of the spectral feature, while $F\lambda$ represents the intensity across the entire wavelength range of interest. $W\lambda$ represents the width of a rectangle which drops to an intensity of zero and has the same integrated area as the true spectral line.

The equivalent width is related to the column density of a line (in an optically thin case) by:

$$W_\lambda = \frac{\pi e^2}{m_e c} N_{J''} f = (8.853 * 10^{-13}) N_{J''} f \quad (cm^{-1}) \tag{B.10}$$

where e is the charge of an electron, m_e is the mass of an electron, c is the speed of light, $N_{J''}$ is the column density in the lower state, and f is the oscillator strength given by:

$$f = \frac{Ac}{(8.852 * 10^{-13}) 8\pi\nu^2} \frac{g_{up}}{g_{low}} \tag{B.11}$$

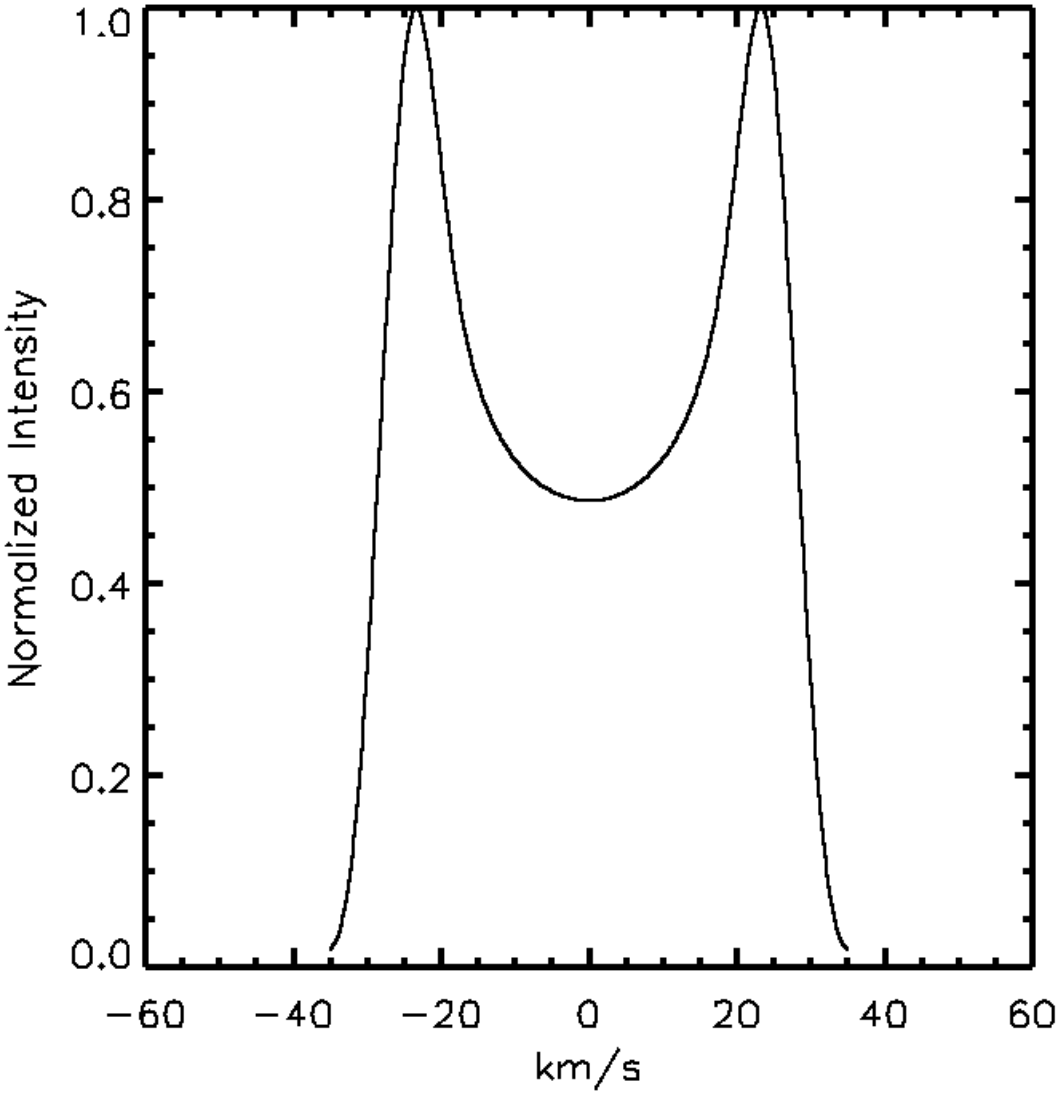

Figure B.1. An example of the double peaked line profile of protoplanetary disk emission. The two peaks are a result of the Doppler shift caused by the rotation of disk material.

where A is the Einstein coefficient for spontaneous emission, ν is the frequency, and g_{up} and g_{low} are the upper and lower state degeneracies. The column density in the lower state can be related to the total column density for a molecule with the fractional population ($N_{J'',rel}$) given by:

$$\mathrm{N}_{\mathrm{J''rel}} = g_{low}\frac{e^{-hcE_{low}/kT_{rot}}}{Q_{tot}} \tag{B.12}$$

where h is Planck's constant, E_{low} is the lower state energy, k is Boltzmann's constant, T_{rot} is the rotational temperature, and Q_{tot} is the total partition function. The total column density can then be calculated with:

$$N_{tot} = \frac{N_{J''}}{N_{J'',rel}} = \frac{W_{\lambda}}{(8.853*10^{-13})\,f}\,\frac{Q_{tot}}{g_{low}e^{-hcE_{low}/kT_{rot}}} \tag{B.13}$$

To determine rotational temperature, synthetic models were generated from 70 – 3000 K. Since the absorption lines were well described by a Gaussian line profile, the models were convolved to a Gaussian profile shape with a width that was varied to fit the observed spectral features. Keplerian rotation of gas in a disk results in an emission profile that is broad and double peaked (see Figure B.1 and Section 4).

With the model convolved to the appropriate line shape, regions were selected to fit the model to the observed data. A similar fitting routine as discussed in Section B.1 was used to determine the best-fit temperature and column density.

BIBLIOGRAPHY

Acke, B., van den Ancker, M. E., & Dullemond, C. P. 2005, A&A, 436, 209

A'Hearn M. F., Feaga L. M., Keller H. U., et al. 2012, ApJ, 758, 29

Ahn, C. P., Alexandroff, R., Allende Prieto, C., et al. 2012, ApJS, 203, 21

Aikawa, Y., & Herbst, E. 1999 A&A, 351, 233

Aime, C., Borgnino, J., Lund, G., et al. 1988, in European Southern Observatory Conference and Workshop Proceedings, Vol. 29, ed. F. Merkle (Garching: ESO), 249

Akeson, R. L., et al. 2005, ApJ, 622, 440

Alexander, R. D., Clarke, C. J., Pringle, J. E. 2006, MNRAS, 369, 216

ALMA Partnership et al., 2015, ApJ, 808, L3

Andrews, S. M., & Williams, J. P. 2007, ApJ, 659, 705

Bailey, J. 1998, MNRAS, 301, 161

Ball, P. 2011, Life's Matrix: A Biography of Water

Banzatti, A., Meyer, M. R., Bruderer, S., et al. 2012, ApJ, 742, 90

Bast, J. E., Brown, J. M., Herczeg, G. J., et al. 2011, A&A, 527, A119

Bast, J. E., Lahuis, F., van Dishoeck, E. F., Tielens, A. G. G. M. 2013, A&A, 551, 118

Beckers, J. M. 1982, Opt. Acta, 29, 36

Bergin, E., Calvet, N., D'Alessio, P, Herczeg, G. J. 2003, ApJ, 591, 159

Bertout, C. 1989, ARA&A, 27, 351

Bonev, B. P. 2005, PhD thesis, http://astrobiology.gsfc.nasa.gov/Bonev_thesis.pdf

Boss, A. P. 1998, Annu. Rev. Earth Planet. Sci., 26, 53

Bouvier, J., et al. 1999, A&A, 349, 619

Bouvier, J., et al. 2003, A&A, 409, 169

Bouvier, J., et al., 2007, A&A, 463, 1017

Bouvier, J., Grankin, K., Ellerbroek, L. E., et al. 2013, A&A, 557, 77

Brannigan, E., Takami, M., Chrysostomou, A., et al. 2006, MNRAS, 367, 315

Brauer, F., Henning, T., & Dullemond, C. P. 2008, A&A, 487, L1

Brittain, S. D., Rettig, T. W., Simon, T., and Kulesa, C. 2005, ApJ, 626, 283

Brittain, S. D., Najita, J. R., Carr, J. S., 2009, ApJ, 702, 85

Brown, L. R., Troutman, M. R., Gibb, E. L. 2013, ApJL, 770, L14

Burrows, C. J., Stapelfeldt, K. R., Watson A. M., et al. 1996, ApJ, 473, 437

Carr, J. S., & Najita, J. R. 2008, Science, 319, 1504

Carr, J. S., & Najita, J. R. 2011, ApJ, 733, 102

Casassus, S., van der Plas, G., Perez, S., et al. 2013, Nature, 493, 191

Caselli P., Ceccarelli C., 2012, A&A Rev., 20, 56

Christy J. W., Wellnitz, D. D., & Currie, D. G. 1983, Lowell Obs. Bull., 9, 28

Clarke, C. J., Gendrin, A., Sotomayor, M. 2001, MNRAS, 328, 485

Clough, S. A., Shephard, M. W., Mlawer, E. J., et al. 2005, JQSRT, 91, 233

Cox, A. W., Grady, C. A., Hammel, H. B., et al. 2013, ApJ, 762, 40

Cuzzi, J. N., Hogan, R. C., Shariff, K. 2008, ApJ, 687, 1432

Dipierro, G., Pinilla, P., Lodato, G., and Testi, L. 2015, MNRAS, 451, 974 (a)

Dipierro G., Price, D., Laibe, G., Hirsh, K., Cerioli, A., Lodato, G., 2015, MNRAS, 453, L73 (b)

DiSanti, M. A., Mumma, M. J., Dello Russo, N., et al. 2001, Icar, 153, 361

Donati, J. F., Skeylly, M. B., Bouvier, J., et al. 2010 Mon. Not. R. Astron. Soc., 409, 1347

Dong R., Zhu Z., Whitney B., 2015, ApJ, 809, 93

Doppmann, G. W., Greene, T. P., Covey, K. R., et al. 2005, AJ, 130, 1145

Doppmann, G. W., Najita, J. R., Carr, J. S., Graham, J. R. 2011 ApJ, 738, 112

Drozdovskaya M. N., Walsh C., van Dishoeck E. F., et al. 2016 MNRAS, 462, 977

Dutrey, A., Lecavelier, D. E. A., Augereau, J. C. 2004, Comets II, 81

Encrenaz, T. 2008, ARA&A, 46, 57

Gibb, E. L., Van Brunt, K. A., Brittain, S. D., Rettig, T. W. 2007, ApJ, 660, 1572

Gibb E. L., Bonev, B. P., Villanueva, G., et al. 2012 ApJ, 750, 102

Gibb, E. L. & Horne, D. 2013, ApJ, 776, 28

Glassgold, A. E., Meijerink, R., & Najita, J. R. 2009, ApJ, 701, 142

Gomes R., Levison H. F., Tsiganis K., Morbidelli A., 2005, Nature, 435, 466

Grankin, K. N., Melnikov, S. Y., Bouvier, J., et al. 2007, A&A, 461, 183

Grinin, V. P., Kiselev, N. N., Chernova, G. P., Minikulov, N. K., & Voshchinnikov, N. V. 1991, Ap&SS, 186, 283

Haisch, K. E., Jr, Lada, E. A., Lada, C. J. 2001, ApJ, 553, 153

Hartigan, P., Hartmann, L., Kenyon, S., et al. 1989, ApJS, 70, 899

Hauschildt, P. H., Allard, F., & Baron, E. 1999, ApJ, 512, 377

Heinzeller, D., Nomura, H., Walsh, C., et al. 2011, ApJ, 731, 115

Henning, T., & Semenov, D. 2013 Chemical Reviews, 113, 12, 9016

Herbst, W., Herbst, D. K., Grossman, E. J., & Weinstein, D. 1994, AJ, 108, 1906

Herbst E., van Dishoeck E. F., 2009, ARA&A, 47, 427

Herczeg, G. J., Linksy, J. L., Valenti, J. A., et al. 2002, ApJ, 572, 310

Hogerheijde, M. R., Begin, E. A., Brinch, Christian, et al. 2011, Science, 334, 338

Honda, M., Inoue, A. K., Fukagawa, M., et al. 2009, ApJ, 690, 110

Hueso, R. & Guillot, T. 2005, A&A, 442, 703

Isella, A., Carpenter, J. M., & Sargent, A. I. 2009, ApJ, 701, 260

Johansen, A., Klahr, H., Henning, Th. 2006, ApJ, 636, 1121

Jørgensen, J. K., Favre, C., Bisschop, S. E., et al. 2012, ApJL, 757, L4

Kenyon, S. J. & Hartmann, L. 1987, ApJ, 323, 714

Kurucz, R. L. 1979, ApJS, 40, 1

Kurucz, R. L. 1993, VizieR On-line Data Catalog: VI/39

Lahuis, F., van Dishoeck, E. F., Boogert, A. C. A., et al. 2006, ApJ, 636, 145

Lecar, M., Podolak, M., Saselov, D., Chiang, E. 2006, ApJ, 630, 1115

Maercker, M., Mohamed, S., Vlemmings, W. H. T., Ramstedt, S., et al. 2012, Nature, 490, 232

Mandell, A. M., Bast, J., van Dishoeck, E. F., et al. 2012 ApJ, 747, 92

McCaughrean, M. J. & O'dell, C. R. 1996, AJ, 111, 1977

McLean, I. S., becklin, E. E., Bendiksen, O., et al. 1998, SPIE, 3354, 566

Meijerink, R., Pontoppidan, K. M., Blake, G. A., et al. 2009, ApJ, 704, 1471

Min, M., Dullemond, C. P., Kama, M., Dominik, C. 2011, Icarus, 212, 416

Morbidelli, A., Chambers, J., Lunine, J. I., et al. 2000, M&PS, 35, 1309

Morbidelli A., Levison H. F., Tsiganis K., Gomes R., 2005, Nature, 435, 462

Mumma M. J., Charnley S. B., 2011, ARA&A, 49, 471

Mumma M. J., Weisman P. R., Stern S. A., 1993. In *Protostars and Planets III*, ed. Levy, E. H., Lunine J. I., p. 1177. Tucson: Univ. Ariz. Press

Najita, J. R., A´ da´mkovics, M., & Glassgold, A. E. 2011, ApJ, 743, 147

Najita, J. R., Carr, J. S., Pontoppidan, K. M., et al. 2013, ApJ, 776, 134

Najita, J. R., Corckett, N., Carr, J. S. 2008 ApJ, 687, 1168

Öberg, K. I., Furuya, K., Loomis, R., Aikawa, Y., et al. 2015, ApJ, 810, 112

O'Brien D. P., Morbidelli A., Bottke W. F., 2006, BAAS, 38, 507

O'Brien, D. P., Walsh, K. J., Morbidelli, A., et al. 2014, Icarus, 239, 74

Okuzumi S., Momose M., Sirono S.-i., Kobyashi H., Tanaka H., 2016, ApJ, 821, 82

Padgett, D. L., Brandner, W., Stapelfeldt, K. R., et al. 1999 AJ, 117, 1490

Pinte C., Dent W. R. F., Ménard F., Hales A., Hill T., Cortes P., de Gregorio-Monsalvo I., 2016, ApJ, 816, 25

Pontoppidan, K. M., Blake, G. A., & Smette, A. 2011, ApJ, 733, 84

Preibisch, T., Kim, Y., Favata, F., et al. 2005, ApJS, 160, 401

Raymond, S. N., Quinn, T., & Lunine, J. I. 2004, Icar, 168, 1

Reipurth, B. & Bally, J. 2001, A&A, 39, 403

Reipurth, B. & Heathcote, S. 1991, A&A, 246, 511

Rothman, L. S., Gordon, I. E., Babikov, Y., et al. 2013, JQSRT, 130, 4

Rothman, L.S., Gordon, I.E., Barber, A., et al. 2009, Journal of Quantitative Spectroscopy & Radiative Transfer, 110, 533-572

Salyk, C., Blake, G. A., Boogert, A. C. A., et al. 2011, ApJ, 743, 112

Salyk, C., Pontoppidan, K. M., Blake, G. A., et al. 2008, ApJL, 676, L49

Schindhelm, E., France, K., Herczeg, G. J., et al. 2012, ApJ, 756, 23

Schneider, P. C., France, K., Günther, H. M., et al. 2015, A&A, 584, 51

Shakura, N. I. & Sunyaev, R. A. 1973, A&A, 24, 337

Simon, S. B. & Prato, L. 1995, ApJ, 450, 824

Sitko, M. L., Day, A. N., Kimes, R. L., et al. 2012, ApJ, 745, 29

Smith, N. Bally, J., Licht, D., Walawender, J. 2005, AJ, 129, 382

Sneden, C. 1973, PhD thesis Univ. Texas, Austin

Stapelfeldt, K. R., Krist, J. E., Ménard, F., et al. 1998, ApJ, 502, 65

Terada, H., Tokunaga, A. T., Kobayashi, N., et al. 2007, ApJ, 667, 303

Tornow, C., Gast, P., Motschmann, U., et al. 2014, P&SS, 98, 233

Tsiganis K., Gomes R., Morbidelli A., Levison H. F., 2005, Nature, 435, 459

Valenti, J. A., Basri, G., & Johns, C. M. 1993, AJ, 106, 2024

van der Plas, G., van den Ancker, M. E., Acke, B., et al. 2009, A&A, 500, 1137

van der Tak, F 2011, Proceedings of the Int. Astro. Union, vol 7, 449

van Dishoeck, E. F. & Black, J. H. 1988, ApJ, 334, 771

van Dishoeck, E. F>, Jonkheid, B., van Hemert, M. C. 2006, FaDi, 133, 231

Vicente, S. M., & Alves, J. 2005, A&A, 441, 195

Villanueva, G. L., Mumma, M. J., DiSanti, M. A., et al. 2011, Icarus, 216, 227

Visser, R., van Dishoeck, E. F., Doty, S. D., Dullemond, C. P. 2009, A&A, 495, 881

Visser, R., Doty, S. D., and van Dishoeck, E. F. 2011, A&A, 534, 132

Walsh, C., Miller, T. J., & Nomura, H. 2010 ApJ, 722, 1607

Walsh, C., Nomura, H., van Dishoeck, E. 2015, A&A, 582, A88

Walsh, K. J., Morbidelli, A., Raymond, S. N., O'Brien, D. P., and Mandell, A. M. 2011, Nature, 475, 206

Watson, D M., Calvet, N. P., Fischer, W. J., et al. 2016, ApJ, 828, 52

Whelan, E. & Garcia, P. 2008, Jets from Young Stars II, 742, 123

Whittet, D. C. B. 2002, Dust in the Galactic Environment, 2nd Edition

Willacy, K., & Woods, P. M. 2009, ApJ, 703, 479

Wolk, S. J. & Walter, F. M. 1996, AJ, 111, 2066

Wyatt, M. C. 2008, ARA&A, 46, 339

Yorke, H. W., Bodenheimer, P., Laughlin, G. 1993, ApJ, 411, 274

Zapata, L. A., Loinard, L., Rodriguez, L. F., et al. 2013, ApJL, 764, 14

Zhang K., Blake G. A., Bergin E. A., 2015, ApJ, 806, L7

Zhu, Z., Hartmann, L., Gammie, C. F., et al. 2010, ApJ, 731, 1134

VITA

Logan Ryan Brown received his Bachelor of Science in Physics from the University of Wisconsin Milwaukee in May of 2010. He then went on to receive his Masters in Physics from the University of Missouri St. Louis in May of 2012, and he received his Doctorate of Philosophy in Physics as part of a cooperative between the University of Missouri St. Louis and the Missouri University of Science and Technology in December 2016.